Monte Carlo Studies of Confined Quantum Systems

by

Chongshan Zhang

(Under the direction of David P. Landau)

Abstract

This dissertation describes the studies of two different quantum systems in confined geometries:

The first is a study of the thermal resistivity and its scaling function in quasi-2D ^{4}He systems by Monte Carlo and spin-dynamics simulations. We use the classical 3D XY model on $L \times L \times H$ lattices with $L \gg H$, applying open boundary condition along the H direction and periodic boundary conditions along the L directions. A hybrid Monte Carlo algorithm is adopted to efficiently deal with the critical slowing down and to produce initial states for time integration. The fourth-order Suzuki-Trotter decomposition method of exponential operators is used to solve numerically the coupled equations of motion for each spin. The thermal conductivity is calculated by a dynamic current-current correlation function. Our results show that (i) the simulational data collapse onto a single curve for several values of H and temperature, thus supporting the concept of finite-size scaling theory, and (ii) the calculated scaling function agrees well with the available experimental results for slabs using two free fitting parameters.

The second is to investigate Bose-Einstein condensates in a quasi-1d box trap using the path-integral Monte Carlo method. Recently Bose-Einstein condensates in a quasi-1d optical box trap has been produced in experiments, and the ground state of quasi-1d Bose gases in a hard-wall trap has been analytically studied. To compare with them, we have

used the same geometry, and approximated the trapping potential with Gaussian functions or hard-wall along the boundary of the box. The two-body interaction was described by a hard-sphere potential whose radius equals the s-wave scattering length. We have calculated the density profiles of the systems as a function of the temperature, the strength of the two-body interaction and the number of the atoms. At last, we compared the simulation results with the experimental and analytical results.

INDEX WORDS: Spin lattice model, superfluid ^{4}He, thermal conductivity, thermal resistivity, Monte Carlo, finite-size scaling theory, critical temperature, Bose Einstein condensation, path integral Monte Carlo method, trapping potential, low dimensionality

Monte Carlo Studies of Confined Quantum Systems

by

Chongshan Zhang

B.S., Beijing University, Beijing, China, China, 1988

M.S., The University of Georgia, Athens, GA, 2005

A Dissertation Submitted to the Graduate Faculty

of The University of Georgia in Partial Fulfillment

of the

Requirements for the Degree

Doctor of Philosophy

Athens, Georgia

2006

Monte Carlo Studies of Confined Quantum Systems

by

Chongshan Zhang

Approved:

Major Professor: David P. Landau

Committee: Steven P. Lewis
Robin L. Shelton
Shan-Ho Tsai

Electronic Version Approved:

Maureen Grasso
Dean of the Graduate School
The University of Georgia
August 2006

Dedication

To my dear parents, Benrang Zhang and Fazhen Lu and my loving wife, Ruoyan Zhang

Acknowledgments

I am extremely thankful to my major professor, David P. Landau for his invaluable guidance and encouragement throughout my entire research and academic years. I have learned to analyze problems thoroughly, pay attention to details, and communicate efficiently.

I would also like to thank Steven P. Lewis, Robin L. Shelton and Shan-Ho Tsai for serving on my advisory committee, and for their advice and guidance.

I thank Kwangsik Nho very much, who has given me tremendous advice and help in my academic endeavor.

I should also thank Xiaoliang Zhu and Steven Mitchell for their generous help and discussions.

I thank G. Ahlers for providing experiment data of thermal conductivity and giving us helpful comments and suggestions.

This research was supported in part by NASA under Grant No. NNC04GB24G.

Table of Contents

Chapter 1

General introduction

Bose Einstein Condensation (BEC) was predicted in 1925 by Albert Einstein[1], by generalizing Satyendra Nath Bose's work on the statistical mechanics of (massless) photons to (massive) atoms. Einstein speculated that cooling bosonic atoms to a very low temperature would cause them to fall (or "condense") into the lowest accessible quantum state, resulting in a new form of matter (Fig. 1.1).

The Bose Einstein condensate was first created by Eric Cornell, Carl Wieman, and coworkers at JILA on June 5, 1995[2]. They did this by cooling a dilute vapor consisting of approximately 2000 ^{87}Rb atoms to below 170 nK using a combination of laser cooling and magnetic evaporative cooling. About four months later, an independent effort led by Wolfgang Ketterle at MIT created a condensate made of ^{23}Na[3]. Ketterle's condensate had about a hundred times more atoms, allowing him to obtain several important results such as the observation of quantum mechanical interference between two different condensates.

What is the physics behind BEC in a dilute gas ($na^3 \ll 1$, where $n = N/V$ is the number density and a is the hard core diameter of the bosons)? As we know, in the view of quantum mechanics, like all atoms, Bose atoms in a gas are described by a wavefunction (matter wave) with the wavelength λ related to the atom's momentum $\mathbf{p}$ by

$$\mathbf{p} = m\mathbf{v} = \hbar/\lambda \tag{1.1}$$

where $\hbar$ is the planck's constant, $\mathbf{v}$ is the velocity of atoms. The average atomic kinetic energy is

$$\bar{E} = \frac{1}{2}m\bar{v}^2 = \frac{\bar{p}^2}{2m} \approx k_B T \tag{1.2}$$

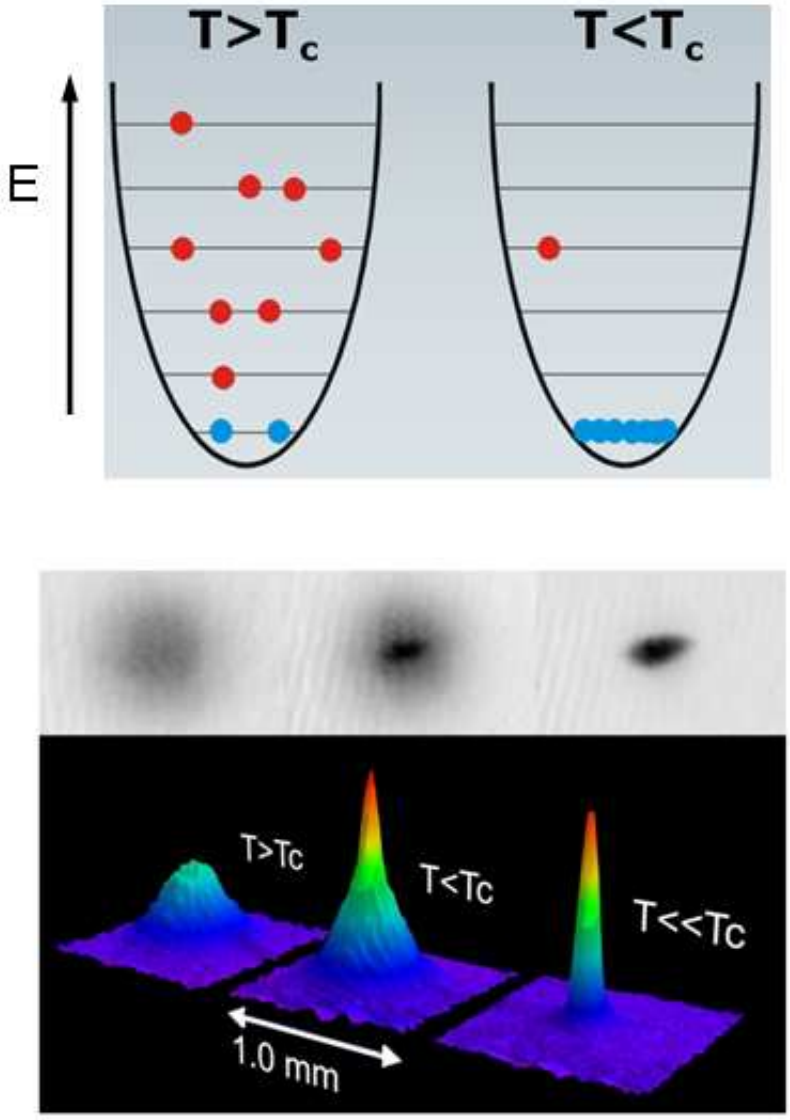

Figure 1.1: BEC. (top) The energy level of atoms as the temperature decreases. (bottom) The momentum density of atoms as the temperature decreases. The three black dots are topview of the momentum density. (From website http://www.colorado.edu/physics/2000/bec/)

where m is the mass of the atoms, k_B is Boltzmann's constant, T is the temperature, and $\bar{v}$, $\bar{p}$ are the average of $|\mathbf{v}|$ and $|\mathbf{p}|$. Thus the de Broglie relation gives

$$\bar{\lambda} \approx \frac{\hbar}{\sqrt{mkT}}. \tag{1.3}$$

When T decreases, the wavelength λ increases. When $\lambda \sim d$, d is the average distance between the atoms in the gas, the matter waves begin to be overlapped, and many Bose atoms start to occupy the lowest energy state. In other words, the system begins to exhibit BEC. At $T = 0$, the $\lambda \to \infty$, all matter waves are overlapped together, and all the Bose atoms in the gas occupy the zero momentum state. Now the system becomes a pure BEC (Fig. 1.2).

A superfluid is a phase of matter characterized by the complete absence of viscosity. This property of certain isotopes was discovered by Pyotr Leonidovich Kapitsa[4], John F. Allen, and Don Misener[5] in 1937. It has been achieved at very low temperatures with at least two isotopes of helium (^{3}He, ^{4}He), one isotope of rubidium, and one isotope of lithium.

The relationship between Bose-Einstein condensation (BEC) [1] and superfluidity was first pointed out by London[6, 7]. He postulated that superfluidity was a consequence of a transition to BEC.

The superfluid phase transition occurs when all the constituent atoms of a sample begin to occupy the same quantum state. This transition happens when the atoms are placed very closely together and cooled down so much that their quantum wave functions begin to overlap (Fig. 1.2, $\lambda \sim d$) and the atoms lose their individual identities, behaving more like a single super-atom than an agglomeration of atoms.

It is found that in a confined system, i.e. dimensionally reduced system, the properties of BEC and superfluidity may be very different from their three-dimensional (3D) counterparts due to the enhanced importance of phase fluctuations.[8, 9] For example, in a spatially homogeneous infinite system a one-dimensional (1D) Bose gas does not exhibit BEC, even at zero temperature; and in two dimensions (2D) BEC exists only at zero temperature[10]. Nonetheless, a dilute 2D Bose gas undergoes a superfluid phase transition at a finite critical

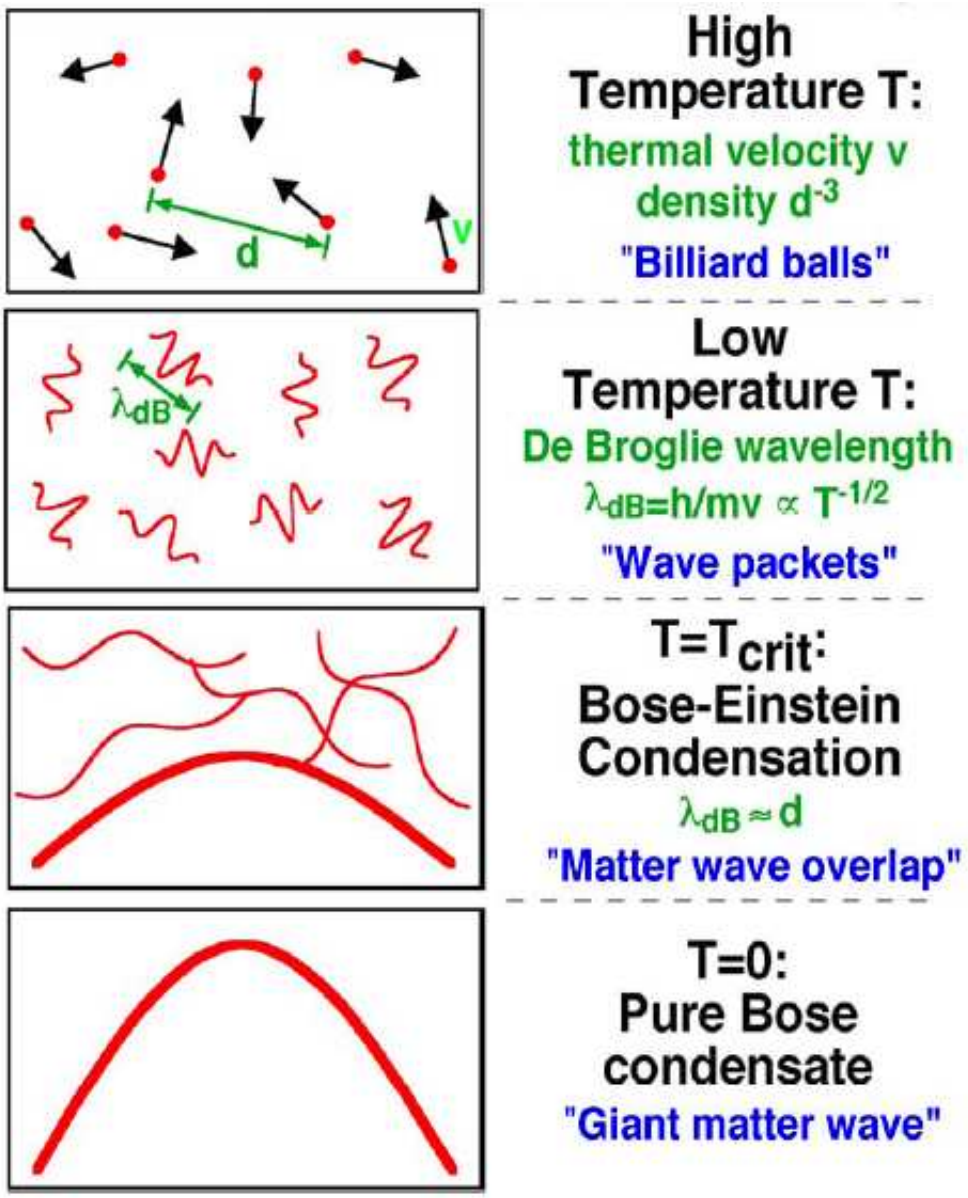

Figure 1.2: BEC – Matter wave overlap. In the view of quantum mechanics, atoms (matter) have properties of both waves and particles. At high temperature, particle nature (dots) dominate. As the temperature decrease, wave nature (curves) exhibits. When the temperature approaches critical temperature, the wave dominated and overlap. When the temperature = 0, wavelength becomes longest. (From website http://online.itp.ucsb.edu/plecture/ketterle, Dr. Ketterle's homepage)

temperature. Another example, at the λ transition, the conductivity of bulk superfluid ^{4}He is infinite. However if the superfluid ^{4}He is in a confined geometry, its conductivity becomes finite because the correlation length is cut off by the surface of the system.

To analyze the effect of finite size scaling of superfluid and BEC systems, first, we study the finite-size effect of thermal resistivity of superfluid ^{4}He in a quasi-2d geometry using Monte Carlo and spin-dynamics simulations with an XY spin model. Second, we study Bose-Einstein condensation in a quasi-1D box boundary trap using the path-integral Monte Carlo method.

Part I

Finite-size effects on the thermal resistivity of ^{4}He in restricted geometries

ABSTRACT

The thermal resistivity and its scaling function in quasi-2D ^{4}He systems are studied by Monte Carlo and spin-dynamics simulations. We use the classical XY model on $L \times L \times H$ lattices with $L \gg H$, applying an open boundary condition along the H direction and periodic boundary conditions along the L directions. A hybrid Monte Carlo algorithm is adopted to efficiently deal with the critical slowing down and to produce initial states for time integration. The fourth-order Suzuki-Trotter decomposition method of exponential operators is used to solve numerically the coupled equations of motion for each spin. The thermal conductivity is calculated by a dynamic current-current correlation function. Our results show that (i) the simulational data collapse onto a single curve for several values of H and temperature, thus supporting the concept of finite-size scaling theory, and (ii) the calculated scaling function agrees well with the available experimental results for slabs using two free fitting parameters.

Chapter 2

Introduction

The atoms of ^{4}He (the most abundant isotope of helium) are very simple – two electrons, two protons, and two neutrons, and the interaction between atoms is quite weak. Thus, ^{4}He has extremely low boiling point(5.2 K at 2.264 atm.), and does not solidify at any lower temperature if the pressure is below 2.5MPa (approximately 25 atm). (Figure 2.1).

However, bulk liquid ^{4}He exhibits a second order phase transition at $T_\lambda \approx 2.172$K where it turns superfluid. It is referred as the λ-transition, because the shape of the specific heat curve vs. temperature resembles the Greek letter λ. As indicated in the phase diagram, the superfluid phase (He II) persists all the way to absolute zero. Just as electrons can flow without resistance in a superconductor, atoms can move without viscosity in a superfluid. Similarly the electrical conductivity is infinite in a superconductor, and the thermal conductivity is infinite in a superfluid.

When the temperature approaches T_λ for bulk liquid ^{4}He, the correlation length becomes infinite, and some physical quantities, such as specific heat, the superfluid density, the thermal conductivity, for example, have singularities. However, if liquid ^{4}He is placed in a finite geometry (e.g., a film, a pore, or a box), such quantities cannot diverge near T_λ because the correlation length is limited by the system size.

Physical systems that exhibit a second-order phase transition and that are confined in a finite geometry are thought to be well described by finite-size scaling theory[11] at temperatures close to the critical temperature T_λ. Finite-size scaling theory is based on the idea that Finite-size effects can be observed when the correlation length ξ becomes of the order of the finite system size (i.e., the side of the cube, the thickness of the film, or the diameter of the

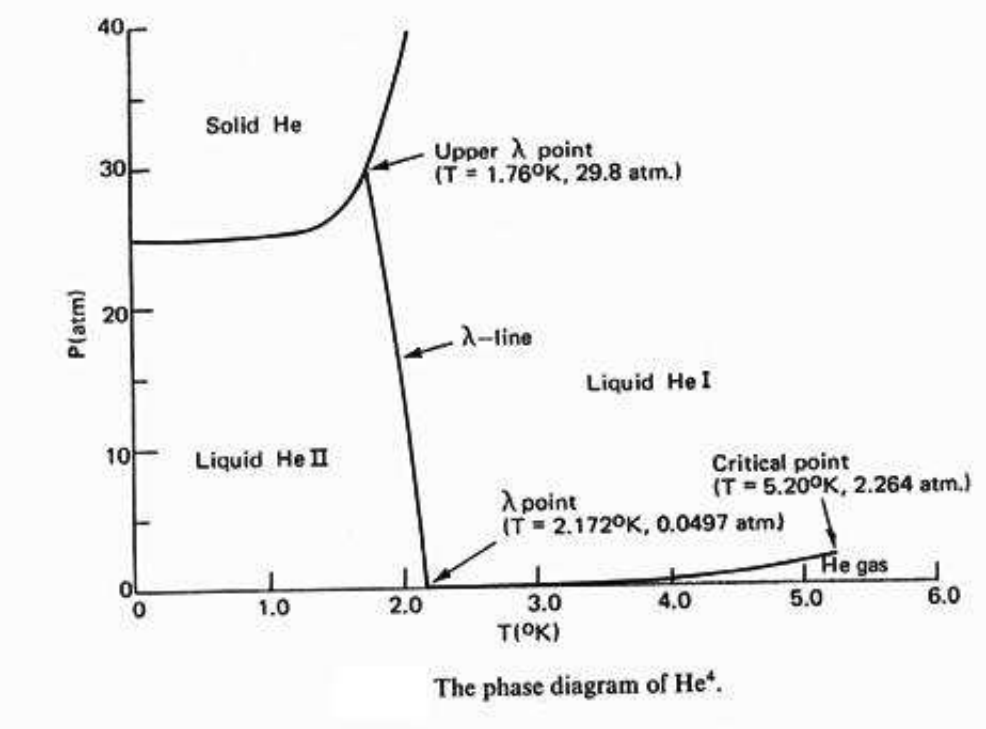

Figure 2.1: Phase diagram for ^{4}He (From website http://www.fluidmech.net/msc/super/super-f.htm, Dr. Cramer's homepage)

pore). For a physical quantity O, this statement can be expressed as follows[12]:

$$\frac{O(\varepsilon, H)}{O(\varepsilon, H=\infty)} = f(x), \tag{2.1}$$

where

$$\varepsilon = \frac{T - T_\lambda}{T_\lambda} \quad \text{and} \quad x = \frac{H}{\xi(\varepsilon, H=\infty)}.$$

Here H denotes the relevant confining length and $\xi(\varepsilon, H = \infty)$ is the correlation length of the bulk system. $f(x)$ is a universal function which does not depend on the microscopic details of the system. It does, however, depend on the observable O, the geometry of the system, and the boundary conditions imposed on the system.

High-resolution measurements of various properties of ^{4}He confined in restricted geometries near the bulk superfluid transition temperature T_λ have been extensively carried out for over three decades [13, 14, 15, 16, 17, 18, 19, 20, 21, 22, 23, 24, 25, 26]. The measurements approach so close to T_λ that the correlation length becomes macroscopic in size. As a result, the whole fluid acts in a correlated way and the values of global properties are changed. This offers an opportunity for testing the finite-size scaling theory which describes the effect of confinement in a finite geometry near a critical point.

Liquid helium ^{4}He has been widely used to examine the validity of the finite-size scaling theory of critical phenomena; sophisticated experimental studies can be carried out in a microgravity environment. For example, Lipa *et al.*[27] measured the specific heat of helium confined in a parallel plate geometry with a spectacular nanokelvin resolution, and the shape of the confining geometry, such as a film, pore, or box, can be designed with such a precision that the relevant confining length is well defined.

For superfluid ^{4}He, the scaling of static properties has been studied experimentally, analytically, and numerically. For example, the specific heat near the superfluid transition of ^{4}He has been measured for confinements which vary by a factor of over 1000, and the data, to a large extent, can be collapsed upon a unique function when properly reduced[13, 14, 15, 16]. Field-theoretical calculations for the standard Landau-Ginzburg free energy functional in

different geometries, with Dirichlet boundary, conditions have been carried out[17, 18, 19], and the results agree with the specific heat measurements[20, 21]. Schultka and Manousakis calculated the superfluid density and the specific heat of ^{4}He in film and pore geometries using Monte-Carlo simulation, and they demonstrated the validity of the finite-size scaling theory[22, 23, 24].

Besides static properties, finite-size scaling theory can also be understood by studying dynamical properties near the critical point. Among them, the thermal conductivity λ of ^{4}He is a good candidate (note that this notiation for thermal conductivity is standard and should not be confused with the λ-point), because it is a measurable property and its bulk transition has been carefully studied both experimentally[28, 29, 30] and theoretically[31]. D. Murphy *et al.*[32] and E. Genio et al.[33] measured the thermal conductivity of liquid ^{4}He confined in "microchannel plates" of thickness 2 mm with holes 0.5 μm and 1 μm in diameter, and their data are consistent with a universal scaling function. Nho and Manousakis[26] studied the thermal conductivity λ of ^{4}He confined in a pore-like geometry and the results of their simulations agree well with experiments. Rather recently, Jerebets et al. measured the thermal conductivity of liquid ^{4}He confined in a film geometry[34]. In this project we will study the thermal conductivity λ of confined helium using Monte Carlo and spin-dynamics methods, calculate the scaling function associated with λ for a film geometry, and compare it with the experimental results.

The remainder of Part I is organized as follows: In Chapter 3, we will present the model, the simulation methods, and the method for extracting the thermal conductivity. In Chapter 4, we will examine the finite-size scaling theory for thermal resistivity and compare our calculated scaling function with experimental results. We summarize our results in Chapter 5.

Chapter 3

Model and simulation method

In this Chapter, first we will show that ^{4} helium is in the XY universality class by introduce Matsubara and Matsuda's work [35] where they shown a lattice model of liquid helium is equivalent with a pseudospin model, thus we can use the XY model to study the critical behavior of the liquid helium. Then we will introduce the XY model and its Hamiltonian. After that, we describe the Monte Carlo and dynamic simulation methods used to study the properties of superfluid ^{4}He. At last, we show how the thermal conductivity is computed in our model.

3.1 Lattice model of liquid helium

The lattice model for classical liquids is a well-known model which provides an adequate approximation for the purpose of taking into consideration the large atomic correlation in the liquid phase. A site of the lattice may be empty or occupied by an atom. The configurations of liquid are described by the distributions of atoms and holes among the lattice points. The fluidity is shown by the change of the distributions of atoms and holes. For example, if a site becomes empty after being occupied while one of its empty nearest neighbors becomes occupied, we can say that an atom "travelled" to the neighbor site from its original site. By excluding multiple occupations of atoms on each lattice point, one can account for the effect of the repulsion between atoms.

In extending this idea of lattice model to quantum liquid such as helium, it is of primary importance to take account of the effect of the zero point motion of the atoms. Since increment in kinetic energy will be caused by localizing each atom in a lattice confuration, it must

be reduced by mixing various configurations. This means that, in the lattice representation, the kinetic energy has large non-diagonal elements such as to produce transitions among various lattice configurations. Thaking consideratin of this effect of the kinetic energy on one hand, and of the excluding effect of the strong repulsion on the other hand, Matsubara and Matsuda [35] constructed a lattice model for liquid helium.

In the model, the liquid is regarded as a lattice composed of atoms and holes. Define operators $a_i^\dagger$ and a_i which create and annihilate an atom at the ith lattice point respectively. For Bose particles, we assume commutation relations,

$$[a_i^\dagger, a_j^\dagger]_- = [a_i, a_j]_- = [a_i, a_j^\dagger]_- = 0 \tag{3.1}$$

for $i \neq j$, and

$$[a_i^\dagger, a_i^\dagger]_+ = [a_i, a_i]_+ = 0, [a_i, a_i^\dagger]_+ = 1 \tag{3.2}$$

to exclude the multiple occupation of atoms at each point.

Then the total potential energy of the system is

$$\Phi = -v_0 \sum_{\langle ij \rangle} a_i^\dagger a_i a_j^\dagger a_j, \tag{3.3}$$

where $-v_0$ is the potential of two atoms which are nearest neighbors, $\langle ij \rangle$ denotes a nearest neighbor pair points. $a_i^\dagger a_i$ represents the number of atoms occupying the i-th point, and therefore the total of number of atoms is given by

$$\sum_i a_i^\dagger a_i = N_0. \tag{3.4}$$

The kinetic energy of the system is

$$K = \frac{\hbar^2}{2md^2} \sum_{\langle ij \rangle} (a_i^\dagger - a_j^\dagger)(a_i - a_j), \tag{3.5}$$

where m is the mass of the particles and d is the distance between nearest neighbors.

Then the Hamiltonian of the system can be written as

$$\mathcal{H}_h = \frac{\hbar^2}{2md^2} \sum_{\langle ij \rangle} (a_i^\dagger - a_j^\dagger)(a_i - a_j) - v_0 \sum_{\langle ij \rangle} a_i^\dagger a_i a_j^\dagger a_j, \tag{3.6}$$

and its grand partition function is

$$Z_h = \text{Trace}[\exp(-\alpha \sum_i a_i^\dagger a_i - \beta \mathcal{H}_h)], \tag{3.7}$$

where $\beta = 1/k_B T$, $-\alpha/\beta$ is the chemical potential. From this partition function all thermodynamic quantities are readily calculated.

3.2 Spin-1/2 system

Matsubara and Matsuda[35] then showed that the lattice liquid helium is identical to the spin-1/2 system. Indeed, for a set of N spins, each of which is localized at each lattice point and $S = 1/2$, the spin operators $S_i^{\pm} = S_i^x \pm i S_i^y$ satisfy the following relations:

$$[S_i^+, S_j^+]_- = [S_i^-, S_j^-]_- = [S_i^+, S_j^-]_- = 0 \quad (i \neq j), \tag{3.8}$$

$$[S_i^+, S_i^+]_+ = [S_i^-, S_i^-]_+ = 0, [S_i^+, S_i^-]_+ = 1. \tag{3.9}$$

These are the same as 3.1 and 3.2. Furthermore, S_i^z can be expressed in terms of S_i^+ and S_i^- (set $\hbar = 1$) as

$$S_i^z = S_i^+ S_i^- - 1/2. \tag{3.10}$$

Then there should exist a certain spin system equivalent to the above lattice model by the correspondence $a_i^\dagger \leftrightarrow S_i^+$ and $a_i \leftrightarrow S_i^-$.

Consider a spin system whose Hamiltonian is given by

$$\mathcal{H}_s = -J \sum_{\langle ij \rangle} (S_i^x S_j^x + S_i^y S_j^y) - J' \sum_{\langle ij \rangle} S_i^z S_j^z - h \sum_i S_i^z, \tag{3.11}$$

where the first two terms represent the anisotropic exchange coupling, and the last term is an external magnetic field. Using $S_i^{\pm} = S_i^x \pm i S_i^y$ and $S_i^z = S_i^+ S_i^- - 1/2$, the Hamiltonian can be rewritten as

$$\begin{aligned} \mathcal{H}_s &= J/2 \sum_{\langle ij \rangle} (S_i^+ - S_j^+)(S_i^- - S_j^-) - J' \sum_{\langle ij \rangle} S_i^+ S_i^- S_j^+ S_j^- \\ &\quad -(h + z/2 \cdot J - z/2 \cdot J') \sum_i S_i^+ S_i^- + N/2 \cdot (h - 1/4 \cdot z J'), \end{aligned} \tag{3.12}$$

where z is the number of nearest neighbors. Its partition function is

$$Z_s = \text{Trace}[\exp(-\beta\mathcal{H}_s)]. \tag{3.13}$$

If one compares Eq. 3.6 and 3.7 to Eq. 3.12 and 3.13, it can be found that

$$Z_h = CZ_s, \tag{3.14}$$

if the following identification is made:

$$\begin{aligned} \hbar^2/2md^2 = J/2 \qquad & \qquad v_0 = J' \\ \alpha = -\beta(h + zJ/2 - zJ'/2) \quad & C = \exp[(N/2)\beta(h - zJ'/4)]. \end{aligned} \tag{3.15}$$

As we obtain the partition function of both systems and their relation, the relation between the physical quantities of both systems can be found. For example, the number density in the lattice model can be expressed as

$$\begin{aligned} \rho &= N_0/N = -\frac{1}{N}\frac{\partial}{\partial\alpha}(\log Z_h) = \frac{1}{N}\frac{\partial}{\partial(\beta h)}(\log C + \log Z_s) \\ &= 1/2 + \frac{1}{N}\langle\sum_i S_i^z\rangle = 1/2 + \langle S_i^z\rangle. \end{aligned} \tag{3.16}$$

In other words, we can investigate the lattice liquid Helium by studying the spin-1/2 system, and the properties of liquid Helium can be expressed as the properties of the spin system.

3.3 Universality

As we mentioned, ^{4}He undergoes a second-order phase transition. When approaching the critical point, some observables have singularities. These observables behave as $A(T) \approx (T - T_c)^{\upsilon}$ near T_c for some exponent υ, called a "critical exponent". These critical exponents may take the same values for a large class of physical systems which are very different. This phenomenon is known as universality, and these systems are said to belong to the same universality class.

Universality states that the thermodynamic properties of a system near a phase transition depend only on a small number of features, such as dimensionality and symmetry, and are insensitive to the underlying microscopic properties of the system. For example, the classical Ising model, the XY model and the Heisenberg model each represents a universality class: the Ising ($N = 1$), the XY ($N = 2$) and the Heisenberg ($N = 3$). These universality classes, apart from the spatial dimensionality and the range of the interactions, are characterized by the number of components N of the order parameter, e.g., the magnetization in the case of spin models[36].

3.4 XY MODEL

The XY model may be viewed as a Heisenberg magnet with an easy-plane (xy) anisotropy such that the order parameter has only two components. The spin-1/2 system described in section 3.2 is in the XY universality class[37]. As the lattice liquid Helium model is identical to the spin-1/2 system, it is also in the XY universality class (planar magnet model). Therefore, the liquid ^{4}He should have same critical behavior as the XY model, and the λ transition of ^{4}He can be described by the XY model. Besides this, the spin dynamics for the XY model also describes the critical dynamics of the ^{4}He near the λ line[36, 37]. Therefore, if one studies the transport properties of the XY model near the critical temperature, one should obtain lattice analogs of the corresponding transport properties of ^{4}He near the λ transition.

The Hamiltonian of the XY model on a lattice takes the following form:

$$\mathcal{H} = -J \sum_{\langle ij \rangle} (S_i^x S_j^x + S_i^y S_j^y), \tag{3.17}$$

where J sets the energy scale,$\langle ij \rangle$ denotes a nearest neighbor pair of spins on a simple cubic lattice in three dimensions, and the summation is over all nearest neighbors. In this model, each spin is a classical spin with three components, $\mathbf{S_i} = (S_i^x, S_i^y, S_i^z)$.

In our calculations, we use a film geometry, i.e. a $L \times L \times H$ lattice with $L \gg H$, in order to mimic the experiment. Open boundary conditions are imposed along the confining

dimension (the H direction). In our model the spins at the open boundary have no neighbors outside the confining space. Periodic boundary conditions are used along the large planar dimensions (L direction), because they better approximate the limit $L \to \infty$.

To calculate the thermal conductivity of superfluid Helium, which is a dynamical property of the system, dynamical simulations for the XY model is needed. To provide starting points for the spin dynamics, a sequence of uncorrelated equilibrium configurations are needed. These configurations are obtained from a Monte Carlo simulation using the Hamiltonian given by Eq. 3.17. Then, starting from the equilibrium configurations, we do dynamic simulations.

3.5 Monte Carlo simulation

The Monte Carlo method was named after Monte Carlo, Monaco, where the primary attractions are casinos containing games of chance. In the simulation, the usual motivation for using the Monte Carlo (MC) method stems from the difficulty of directly solving problems with many interacting degrees of freedom. Rather than finding an exact solution, the MC method allows one to stochastically sample a probability distribution P and obtain an ensemble of states. The averages of some properties then can be obtained according to the probability distribution. The precision of the averages should increase as one increases the number of states sampled.

The Monte Carlo methods rely on the ability to generate an ensemble of configurations which are sampled from the probability distribution of interest. The most popular and straightforward way of accomplishing this is the Metropolis sampling method. The transition probability has to satisfy detailed balance

$$P_n W_{n\to m} = P_m W_{m\to n}, \tag{3.18}$$

where P_n is the probability of the system being in state n, and $W_{n\to m}$ is the transition rate for $n \to m$. In a classical system that follows the Boltzmann distribution, P_n is given by

$$P_n = \exp(-E_n/k_BT)/Z, \tag{3.19}$$

where Z is the partition function. So we have

$$\frac{W_{n\to m}}{W_{m\to n}} = \frac{P_m}{P_n} = \exp(-\Delta E/k_BT), \tag{3.20}$$

where $\Delta E = E_m - E_n$. Any transition rate that satisfies detailed balance is acceptable. The first choice of rate that was used in statistical physics is the Metropolis form [38]

$$W_{n\to m} = \exp\left(-\Delta E/k_BT\right), \quad \text{if } \Delta E > 0 \tag{3.21}$$

$$= 1, \quad \text{if } \Delta E < 0 \tag{3.22}$$

where the time unit is set to unity and suppressed in the equations. The recipe for the Metropolis algorithm follows.

1. Choose an initial state
2. Choose a site i
3. Select a new direction for the spin at site i randomly, calculate the energy change ΔE
4. Generate a uniform random number r in the interval $[0, 1]$.
5. If $r < \exp\left(-\Delta E/k_BT\right)$, set the new direction for the spin at site i. Otherwise, keep the old direction.
6. Go to the next site and go to step 3

However the Metropolis method is not efficient near the critical temperature. As the critical temperature is approached, the large spatial correlations which develop have long temporal correlations associated with them as well, and the relaxation time becomes longer. The Wolff cluster method[39] attempts to beat this "critical slowing down" in spin models

on lattices by flipping correlated clusters of spins in an intelligent way instead of simply attempting single spin-flips. The Wolff cluster algorithm can be stated as follows:

1. Randomly choose a site i
2. Flip $\mathbf{S}_i$ to $\mathbf{S}_i - 2(\mathbf{S}_i\mathbf{r})\mathbf{r}$, where $\mathbf{r}$ is a random unit vector
3. Draw bonds to all nearest neighbors of site i, for examle site j, with probability $p = 1 - \exp\{\min[0, 2\beta(\mathbf{r}\cdot\mathbf{S}_i)(\mathbf{r}\cdot\mathbf{S}_j)]\}$, where $\beta = 1/k_BT$. If the bond between site i and site j is drawn, flip $\mathbf{S}_j$ to $\mathbf{S}_j - 2(\mathbf{S}_j\mathbf{r})\mathbf{r}$.
4. If bonds have been drawn to any nearest neighbor site j, draw bonds to all nearest beighbours k of site j in same way with step (3)
5. Repeat step (4) until no more new bonds are created
6. Go to step (1)

Besides the Metropolis and Wolff cluster algorithms, we also consider the overrelaxation algorithm[40], which performs a microcanonical update of the configuration in the following way. The local configurational energy has the functional form of a scalar product of the spins, where according to Eq. 3.17 only the x and y components are involved. With respect to the sum of its nearest neighbor spins, each spin has a transverse component in the XY plane which can be shown as follows:

$$\mathcal{H} = -J\sum_{\langle ij\rangle}(S_i^xS_j^x + S_i^yS_j^y) = -J\sum_i(S_i^x\sum_{j\in\mathrm{NN}(i)}S_j^x + S_i^y\sum_{j\in\mathrm{NN}(i)}S_j^y) \tag{3.23}$$

Let

$$\mathbf{a} = (S_i^x, S_i^y), \mathbf{b} = (\sum_{j\in\mathrm{NN}(i)}S_j^x, \sum_{j\in\mathrm{NN}(i)}S_j^y) \tag{3.24}$$

the transverse component of spin i is

$$\mathbf{a} - \frac{\mathbf{a}\cdot\mathbf{b}}{\mathbf{b}^2}\mathbf{b} \tag{3.25}$$

It is obvious that this transverse component does not enter the scalar product. The overrelaxation algorithm simply scans the lattice sequentially, determines this transverse component for each lattice site and flips its sign. This does not change the local configurational energy ($\Delta E = 0$) and by virtue of the usual Metropolis acceptance function $f(\beta\Delta E) = \min[\exp(\beta\Delta E), 1]$ the update is always accepted. Along with this simple operation, the sign of S_i^z is flipped with probability 1/2 at each lattice site which according to Eq. 3.17 also does not change the energy of the configuration. This overrelaxation algorithm quite efficiently decorrelates subsequent configurations over a wider range of temperatures around the critical point than does the Wolff algorithm.

In our simulation, the configurations are obtained from a Monte Carlo simulation using the Hamiltonian given by Eq. 3.17. We use a hybrid Monte Carlo procedure[36], which consists of 10 updates (MCCMOCMCCO), where M is a Metropolis update[38], C is a Wolff cluster update[39] and O is an over-relaxation update[40].

The Metropolis algorithm updates the lattice sequentially in the standard way as described above. The Wolff algorithm also works the standard way except that only the x and y components of the spins are used for the cluster growth. This means that a cluster update never changes the z component of any spin, so that the Wolff algorithm is nonergodic in this case. Our cluster update is still a valid Monte Carlo step in the sense that it fulfills detailed balance, however, in order to provide a valid Monte Carlo algorithm it has to be used together with the Metropolis algorithm described above in a hybrid fashion.

Using the hybrid algorithm described above, we generate approximately 1000 uncorrelated configurations from the equilibrium canonical ensemble at a given temperature. To be sure that equilibrium is reached, 10000 hybrid Monte Carlo steps are discarded to obtain the first configuration. Then to make sure the configurations are uncorrelated, 1000 hybrid Monte Carlo steps are discarded between configurations.

The random number generator we use is the shift register generator R1279 given by the recursion relation,

$$X_n = X_{n-1063}.\text{XOR}.X_{n-1279}, \tag{3.26}$$

where $X_n = (16807X_{n-1})mod(2^31 - 1)$ and .XOR. is the bitwise exclusive OR operator. It is known that random number generators can cause systematic errors in combination with the Wolff algorithm. However, for lags pair as large as the ones used here (1063, 1279), these errors will be far smaller than typical statistical errors[41]. They are further reduced by the hybrid algorithm[42].

3.6 Dynamic simulation — decomposition method

After we obtain uncorrelated equilibrium configurations, we do a dynamic simulation starting from each configuration. The spin dynamics of the XY model is defined by the equations of motion, which are given as follows[36, 37]:

$$\frac{\mathrm{d}}{\mathrm{d}t}\mathbf{S_i} = \frac{\partial \mathcal{H}}{\partial \mathbf{S_i}} \times \mathbf{S_i}, \tag{3.27}$$

where H is the Hamiltonian defined by Eq. 3.17. One may interpret Eq. 3.27 as the direct classical analog of the Heisenberg equations of motion for spin operators, where $\hbar = 1$ so that energies and frequencies are measured in the same units. The quantities $M_x = \sum_i S_i^x$ and $M_y = \sum_i S_i^y$ are components of the order parameter of the XY model and they are not conserved under the dynamics given by Eq. 3.27. The out-of-plane component $M_z = \sum_i S_i^z$ is the conserved quantity because of the symmetries of the Hamiltonian in Eq. 3.17.

To do the dynamic simulation according to Eq. 3.27, we need to perform numerical integration of these equations of motion starting from a particular initial spin configuration. It is desirable to do the integration with the biggest possible time step taking the CPU time in account. However, using standard methods the conservation laws of the dynamics cannot be observed within some accuracy if the time step is big. To overcome this restriction, we

use a recently developed decomposition method[43, 44], which follows the Suzuki-Trotter decomposition methods.

Because we only think about the interaction between nearest neighbors, the lattice can be decomposed into two sublattices such that the rotation of a spin only depends on the neighbor spins which are all located on the other sublattice. Denoting the two sublattices by $\mathcal{A}$ and $\mathcal{B}$ respectively, we can write Eq. 3.27 in the form

$$\begin{aligned} \frac{\mathrm{d}}{\mathrm{d}t}\mathbf{S}_{i\in\mathcal{A}} &= \Omega_{\mathcal{B}}[\{\mathbf{S}\}] \times \mathbf{S}_{i\in\mathcal{A}} \\ \frac{\mathrm{d}}{\mathrm{d}t}\mathbf{S}_{i\in\mathcal{B}} &= \Omega_{\mathcal{A}}[\{\mathbf{S}\}] \times \mathbf{S}_{i\in\mathcal{B}}, \end{aligned} \tag{3.28}$$

where $\Omega_{\mathcal{A}}[\{\mathbf{S}\}]$ and $\Omega_{\mathcal{B}}[\{\mathbf{S}\}]$ denote the local fields produced by the spins on sublattice $\mathcal{A}$ and $\mathcal{B}$, respectively. Either of the equations in Eq. 3.28 reduces to a linear system of differential equations if the spins on the other sublattice are kept fixed. This suggests an alternating update scheme, i.e., the spins in $\mathbf{S}_{i\in\mathcal{A}}$ are rotated for the given values of spins in $\mathbf{S}_{i\in\mathcal{B}}$ and vice versa. From equation Eq. 3.17 and Eq. 3.27 we therefore find that the energy is exactly conserved during this alternating update scheme.

According to M. Krech et al. [44], the update of a configuration from time t to $t + \delta t$ is determined by an exponential operator $e^{(A+B)\delta t}$, where A and B are matrices composed of spins in sublattices $\mathcal{A}$ and $\mathcal{B}$ respectively. Although the exponential operator $e^{(A+B)\delta t}$ rotates each spin of the configuration it has no simple explicit form, because the rotation axis for each spin depends on the configuration itself and is therefore not known a priori. However, the operators $e^{A\delta t}$ and $e^{B\delta t}$ do have a simple explicit form.

The update scheme for the integration of Eq. 3.28 now amounts to the replacement $e^{(A+B)\delta t} \to e^{A\delta t}e^{B\delta t}$, which is only correct up to terms of the order $(\delta t)^2$. This is not insufficient for practical purposes.

To overcome this shortcoming, we employ higher order Suzuki-Trotter decompositions of the exponential operator $e^{(A+B)\delta t}$ to increase the order of the local truncation error of the

algorithm. The second order decomposition[45] is given as

$$e^{(A+B)\delta t} = e^{A\delta t/2} e^{B\delta t} e^{A\delta t/2} + O(\delta t^3). \tag{3.29}$$

Furthermore, the fourth order decomposition[45] is given as

$$e^{(A+B)\delta t} = \prod_{i=1}^{5} e^{p_i A\delta t/2} e^{p_i B\delta t} e^{p_i A\delta t/2} + O(\delta t^5), \tag{3.30}$$

with the parameters

$$p_1 = p_2 = p_4 = p_5 \equiv p = 1/(4 - 4^{1/3}) \text{ and } p_3 = 1 - 4p. \tag{3.31}$$

In our simulation, we use the fourth order decomposition.

3.7 Thermal resistivity

As mentioned in previous chapter, the transport properties of the XY model near the critical point provide lattice analogues of the corresponding transport coefficients of ^{4}He near the λ transition. The conserved out-of-plane component M_z of the magnetization is the lattice analog of the entropy density in ^{4}He, and its associated transport coefficient therefore corresponds to the thermal conductivity of ^{4}He, which is of experimental interest. The thermal conductivity λ of liquid ^{4}He at a given temperature T can be estimated using the dynamic current-current correlation function for the XY model[36, 46]

$$\lambda \propto \int_0^\infty dt \sum_i < j_0^z(0) j_i^z(t) >, \tag{3.32}$$

where the j_i^z is the z component of the current density $\mathbf{j_i}$.

In order to identify the current density j_i^z we reexamine the z component of the equation of motion (Eq. 3.27) which reads,

$$\frac{d}{dt} S_i^z = -J \sum_{l \in NN(i)} (S_l^x S_i^y - S_l^y S_i^x), \tag{3.33}$$

where $NN(i)$ denotes the nearest neighbors of lattice site i, the sum is over all nearest neighbors of lattice site i.

Using the density $\rho_i \equiv S_k^z$ and the equation of continuity $\partial\rho_i/\partial t = -\nabla \cdot \mathbf{j}_k$, Eq. 3.33 can be rewritten as

$$\nabla \cdot \mathbf{j}_i = J \sum_{l \in NN(i)} (S_l^x S_i^y - S_l^y S_i^x), \tag{3.34}$$

Suppose we define the kth component $j_i^k (k = x, y, z)$ of the current density $\mathbf{j}_i$ associated with the lattice point i by

$$j_i^k = J(S_i^y S_{i+e_k}^x - S_i^x S_{i+e_k}^y), \tag{3.35}$$

where the notion $i + e_k$ denotes the nearest neighbor of the lattice site i in the kth lattice direction. For the case of the simple cubic lattice studied here, e_x, e_y and e_z can be visualized as the unit vectors of a Cartesian coordinate system aligned with the lattice. Then the lattice divergence of the current density according to Eq. 3.35 at lattice site i is given by

$$\nabla \cdot \mathbf{j}_i = \sum_{k=x,y,z} (j_i^k - j_{i-e_k}^k) = J \sum_{l \in NN(i)} (S_l^x S_i^y - S_l^y S_i^x), \tag{3.36}$$

which is just the right-hand side of Eq. 3.34. Note that the lattice spaceing has been set to unity. In other word, the current density $\mathbf{j}_i$ defined in Eq. 3.35 satisfies Eq. 3.34, thus Eq. 3.33. As the current density can be expressed in terms of spins, the thermal conductivity can be obtained according to Eq. 3.32.

The integration with the decomposition method is carried out to a maximum time $t_{\max}$ (typically of the order of $t_{\max} = 200/J$), with time step $\delta t = 0.1/J$, to make sure that we determine the real-time history of every configuration within a sufficiently long interval of time ($0 \leq t \leq t_{\max}$). Finally, we compute the average of a time-dependent observable (such as the current-current correlation function) over all results relative to all the independent initial equilibrium configurations generated via the hybrid Monte Carlo procedure.

The simulation has been performed on the IBM p655 high performance computer in the Research Computing Center at University of Georgia. The calculation runs on multiple processors with different random number simultaneously. Compared to calculating static critical properties, the computation of dynamical properties needs far more CPU time. To

obtain a value of λ for system size $10 \times 50 \times 50$, the CPU time is about 3×10^6s. All error bars for the thermal resistivity correspond to one standard deviation.

Chapter 4

Results

In this section, we calculate the thermal resistivity, examine its scaling behavior with respect to H, and compare the scaling function with the experimental results.

4.1 Results of thermal resistivity

For a film geometry, $L \times L \times H$, it is better to keep H finite and let $L \to \infty$ such that the system cannot feel the effect of L for any temperature. In other words, we wish the correlation length to be larger than H, but always less than L for any temperature. We can realize this by performing an extrapolation to the infinite limit from the results on finite L. However, we do not have to do this, because we find that by applying periodic boundary conditions along the directions of L, the finite-size effects due to L are already insignificant as long as $L \geq 5H$ (see Fig. 4.1). As an example, Fig. 4.1 shows the thermal resisitivity $R(\varepsilon, H) = 1/\lambda(\varepsilon, H)$ for film lattices as a function of L/H for $H = 6$ at the critical temperature, where the correlation length is infinite. From Fig. 4.1, we can see that within error bars, the results of thermal resistivity are same for $L/H \geq 5$.

Fig. 4.2 shows some of our results of the thermal resistivity $R(T, H)$ as a function of temperature T for various lattice sizes H. The bulk transition temperature $T_\lambda = 1.5518(2)$ is obtained from Monte Carlo simulation[47]. Near T_λ, the data show strong effects of confinement. The smallest size shows the greatest rounding of transition and the thermal resistivity is biggest for smallest size at the critical temperature. At high temperature, the thermal resistivity for different H has no obvious difference within error bars, because $\xi(\varepsilon) < H$.

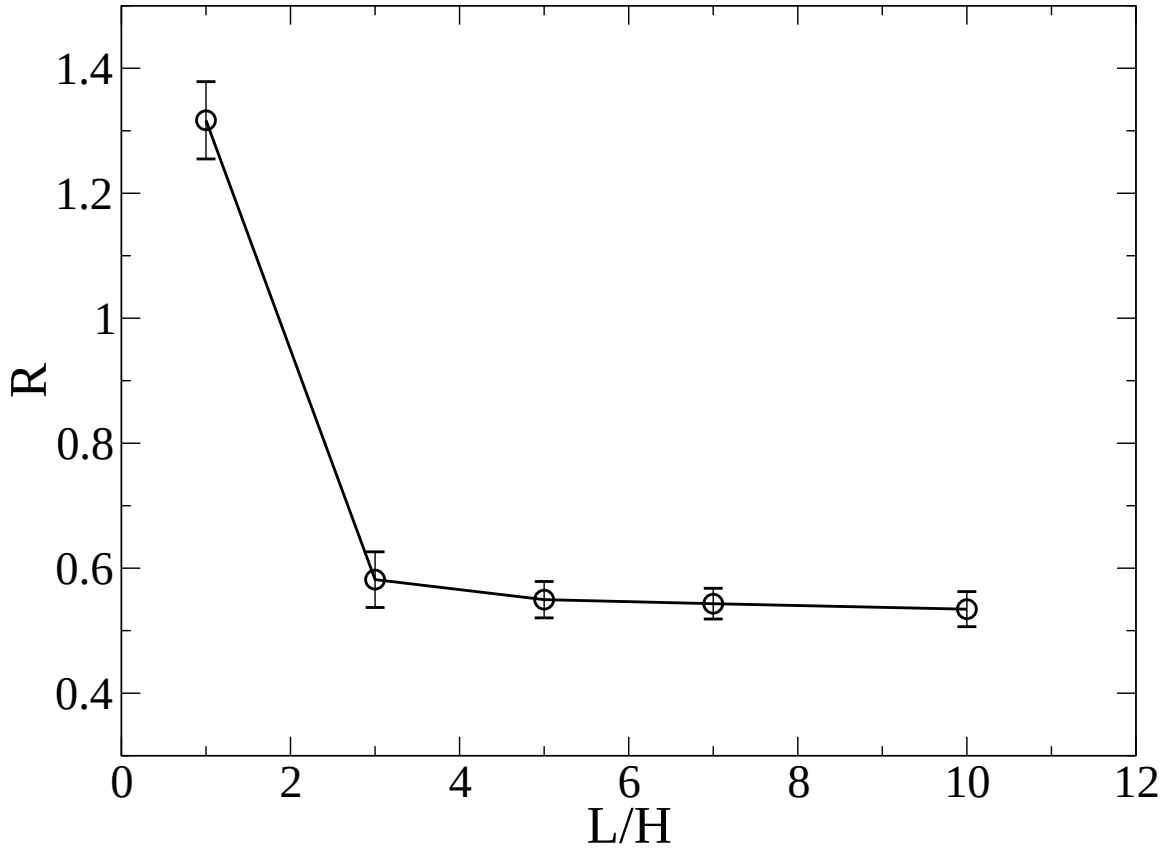

Figure 4.1: The thermal resistivity with a fixed $H = 6$ at T_λ as a function of L/H.

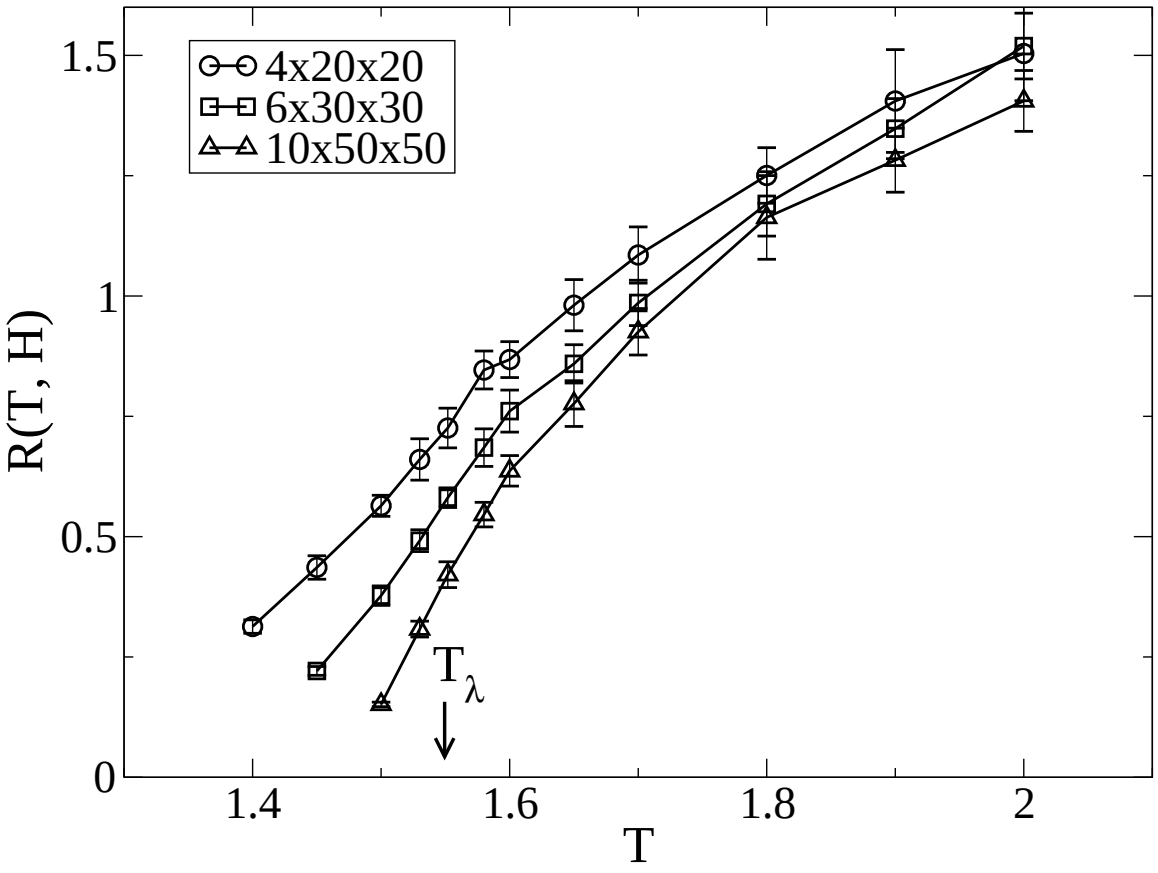

Figure 4.2: Thermal resistivity $R(T, H)$ of the XY model versus temperature for film geometry with sizes that correspond to H =4, 6, 10 and $L = 5H$. The bulk critical temperature $T_\lambda = 1.5518$[47] is also shown.

4.2 Finite-size scaling

Now we would like to check the finite-size scaling hypothesis[11] for the thermal resistivity and to compare our results with the existing experimental results[34]. Consistent with experiment[28], the dependence upon ε of the bulk thermal resistivity can be described by a power-law

$$R(\varepsilon, H \to \infty) = R_0 \varepsilon^{\chi}, \tag{4.1}$$

where χ is an effective critical exponent of the thermal resistivity. Data from experiments as well as results for a number of exactly soluble models show that the dependence upon ε of the correlation length can be described by a power-law[48]

$$\xi(\varepsilon) = \xi_0 \varepsilon^{-\nu}, \tag{4.2}$$

where ν is the critical exponent of the correlation length. According to Eq. 2.1 , the finite-size scaling expression for the thermal resistivity $R(\varepsilon, H)$ is

$$R(\varepsilon, H) = R(\varepsilon, H \to \infty) f_1(H/\xi). \tag{4.3}$$

Redefiningg

$$f_2(H/\xi) = (H/\xi)^{\chi/\nu} f_1(H/\xi), \tag{4.4}$$

and using Eq. 4.1 and Eq. 4.2, Eq. 4.3 can be writen as

$$R(\varepsilon, H) = R_0 \varepsilon^{\chi} (H/\xi)^{-\chi/\nu} f_2(H/\xi) = R_0 (H/\xi_0)^{-\chi/\nu} f_2(H\varepsilon^{\nu}/\xi_0) \tag{4.5}$$

i.e.

$$R(\varepsilon, H) H^{\chi/\nu} = R_0 {\xi_0}^{\chi/\nu} f_2[(H^{1/\nu}\varepsilon)^{\nu}/\xi_0] = g(\varepsilon H^{1/\nu}) \tag{4.6}$$

where $g(x) = g(\varepsilon H^{1/\nu})$ is a universal function.

In this dissertation, we use the critical exponent of the correlation length $\nu = 0.6705$ as determined by Goldner and Ahlers in their experiments[49]. For χ, the dynamic scaling theory[50] predicted an asymptotic value $\chi = \nu/2$. However, Ahlers used the experimental data to determine an effective critical exponent $\chi = 0.4397$ at saturated vapor pressure using the power-law fitting (see Eq. 4.1) for $3 \times 10^{-6} \leq \varepsilon \leq 2 \times 10^{-4}$, and in this fitting, there is no systematical deviation from the power-law fitting, i.e. no need for the correction terms[51]. In other words, the effective critical exponent $\chi = 0.4397$ is valid for whole range $3 \times 10^{-6} \leq \varepsilon \leq 2 \times 10^{-4}$. Furthermore, renormalization group calculations[31] agree with the experimental data of Ahlers, but not with the dynamic scaling prediction. The recent renormalization group calculations[32, 52] have yielded results for $\lambda(\varepsilon, H)$, $\lambda(\varepsilon, H) = 1/R(\varepsilon, H)$, and the slope of the curve of $\log(\lambda)$ vs $\log(1/H)$ at $\varepsilon = 0$ gives an effective exponent which is very close to the experimental value of Ahlers.

If the finte-size scaling theory (Eq. 2.1) well describes the confined physics system, according to Eq. 4.3, the plot of the thermal resistivity scaling function $g(x) = R(\varepsilon, H)H^{\chi/\nu}$ vs $x = \varepsilon H^{1/\nu}$ for different values of ε and H should be a single curve. Fig. 4.3 shows a scaling plot of $g(x)$ versus x with $\chi = 0.4397$, where the reduced temperature is taken relative to the bulk transition temperature T_λ. From Fig. 4.3, we can find that our simulational data collapse onto one single curve for a wide range of values of H and ε, thus supporting the concept of finite-size scaling theory over a factor of 3.5 in H.

In Fig. 4.3 we also compare our scaling function $g(x)$ with the experimental data obtained by Jerebets et al.[34], represented by a solid line. In the simulation, we use reduced units for the interaction constant J, the temperature ε, the spin $\mathbf{S}$ and the distance of nearest neighbor spins on the lattice, therefore, the x and $g(x)$ also have reduced units. In order to compare with the experimental data, we have to used two multiplicative constants as free fitting parameters, one multiplying the scale of the x-axis and another the scale of the y-axis. The two parameter fitting does not change the shape of the scaling function. Figure 4.3 shows that the agreement between simulation and experiment is quite good except for

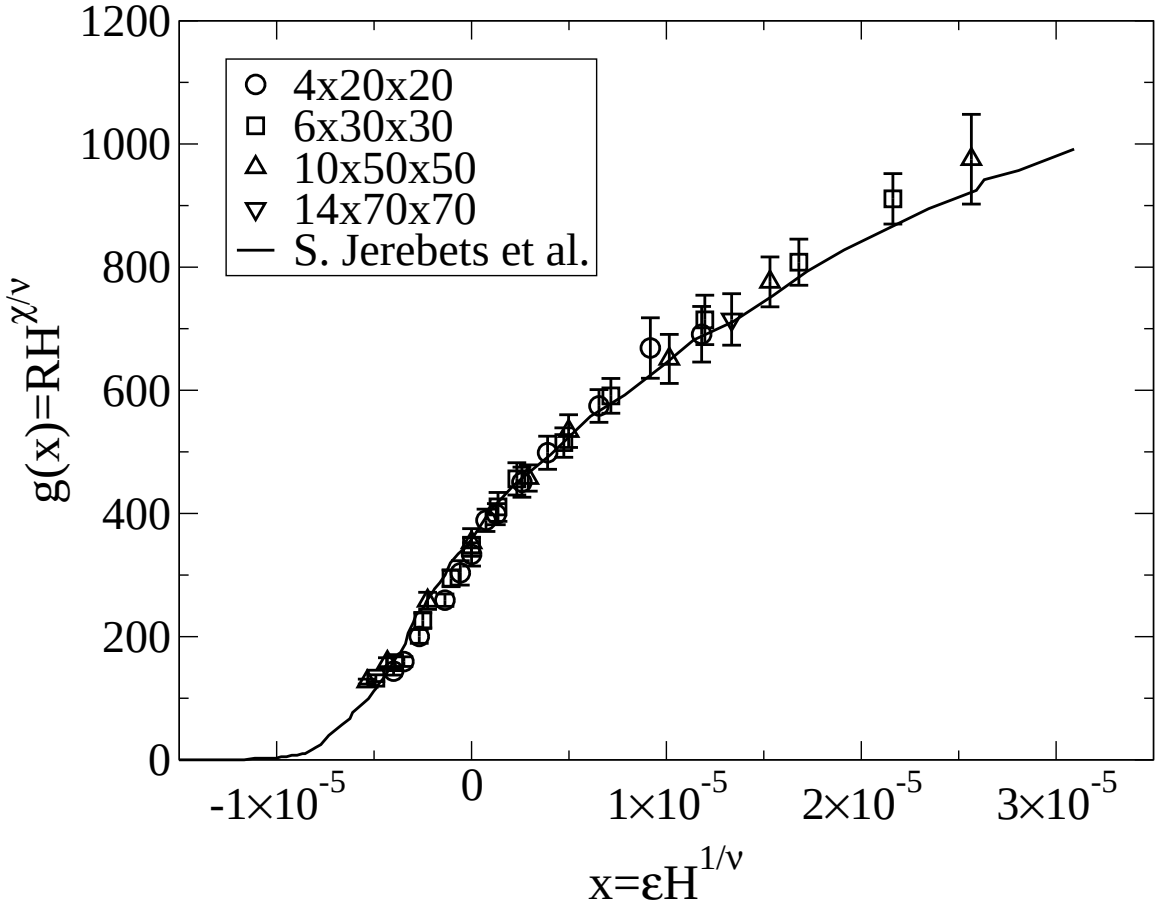

Figure 4.3: The universal function $g(x)$ obtained for film geometry with $\chi = 0.4397$. The solid line represents the available experimental results for film geometry[34]. R is measured in units of cmK/W and H is measured in units of μm. To compare the results of simulation and experiment, we applied two free-parameter adjustments to the simulation results.

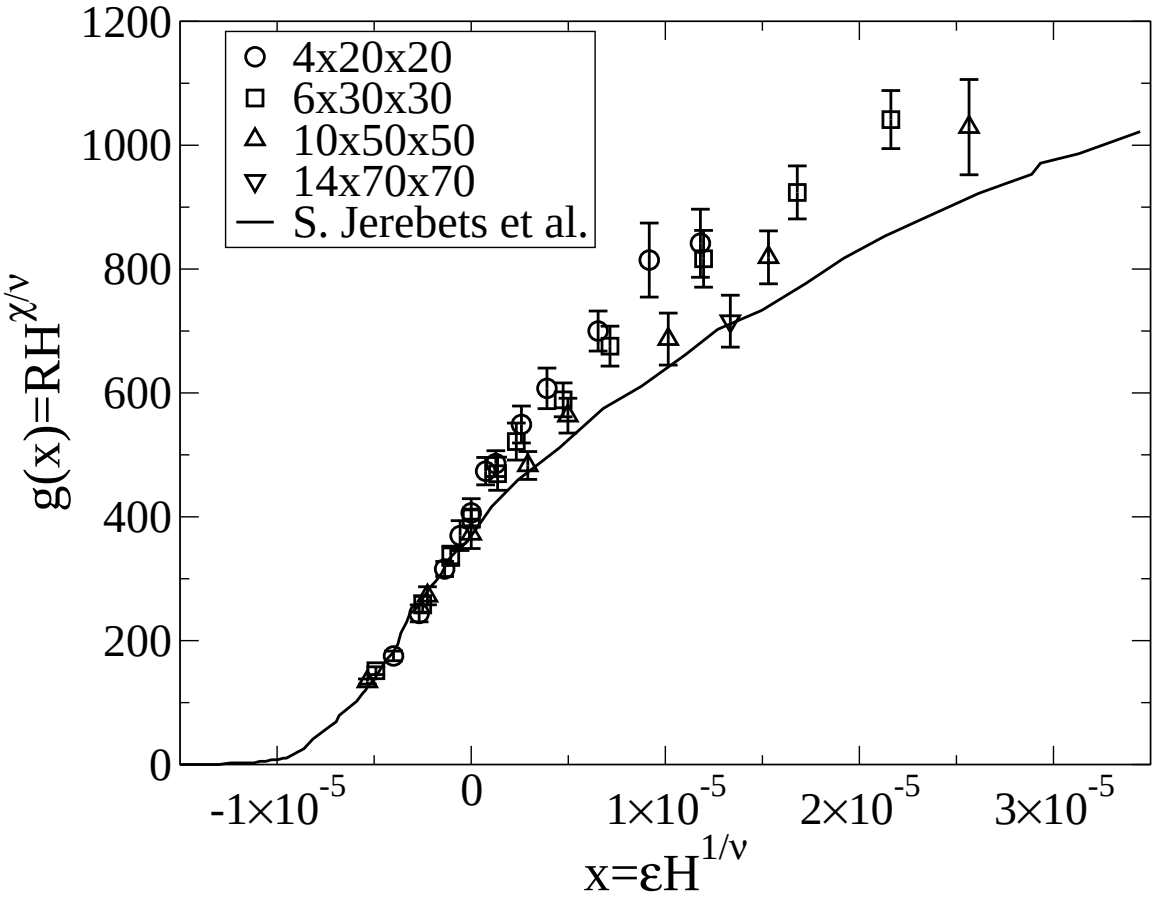

Figure 4.4: The universal function $g(x)$ obtained for film geometry with $\chi = \nu/2 = 0.335$. The solid line represents the available experimental results for film geometry[34]. R is measured in units of cmK/W and H is measured in units of μm. To compare the results of simulation and experiment, we applied two free-parameter adjustments to the simulation results.

$x < -0.4 \times 10^{-5}$. The difference for $x < -0.4 \times 10^{-5}$ may suggest a breakdown of finite-size scaling in the superfluid phase as in the experiment[51] in quasi-1D.

Fig. 4.4 shows a scaling plot of $g(x)$ versus x with $\chi = \nu/2 = 0.335$. From Fig. 4.4, we can find that the simulation data collapse onto one single curve when $x < -0.4 \times 10^{-5}$. However, as x increase, the scaling does not work well for different H. We also compare our scaling function $g(x)$ with the experimental data, the solid line in Fig. 4.4. In the range

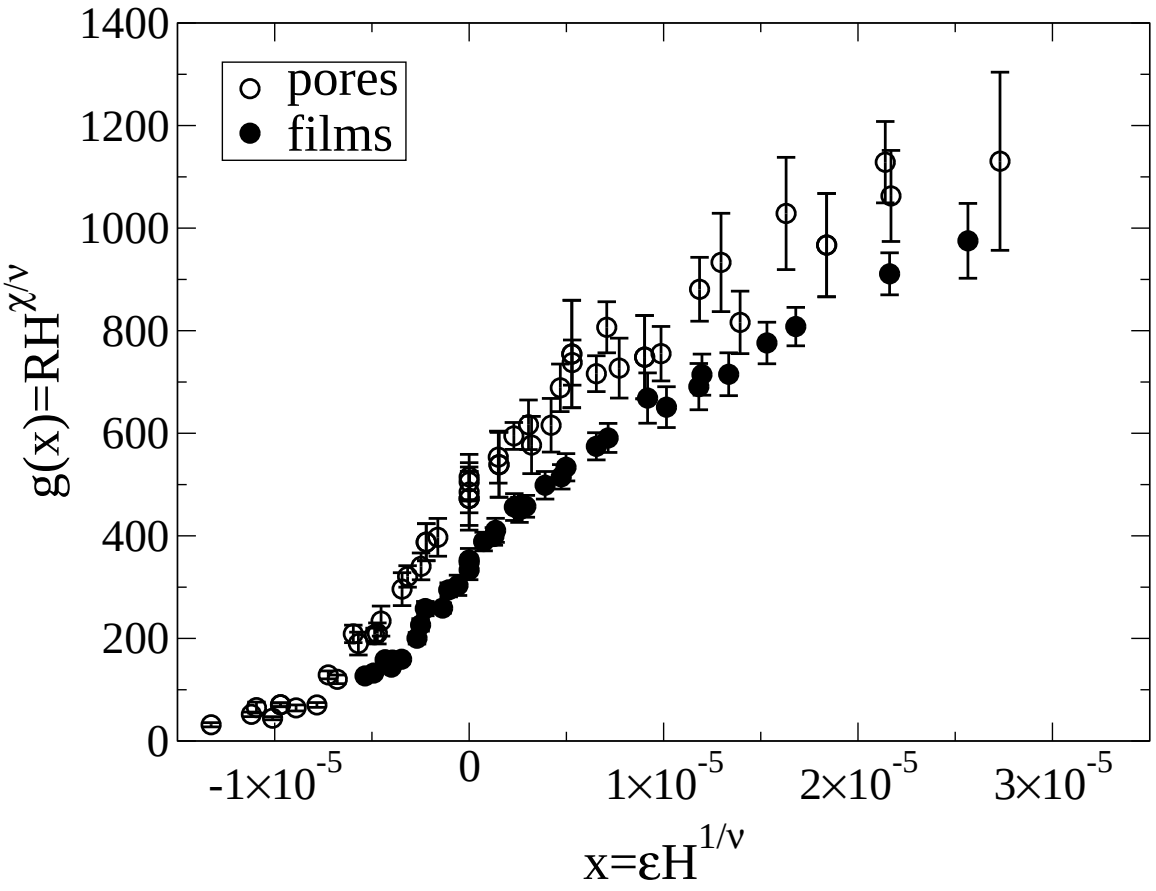

Figure 4.5: Comparison of the finite-size scaling functions $g(x)$ for films and pores as determined from computer simulations.. The units of R and H are same as in Fig. 4.3.

$x < -0.4 \times 10^{-5}$, the agreement between simulation and experiment is good. For the larger x, the simulation does not agree with the experiment. This may suggest that the χ has different values for different x. As shown in Fig. 4.3 and Fig. 4.4, the agreement between simulation and experiment is better using $\chi = \nu/2 = 0.335$ than using $\chi = 0.4397$ in the range $x < -0.4 \times 10^{-5}$, while $\chi = 0.4397$ is more suitable in range $x > -0.4 \times 10^{-5}$.

The geometry is one of the important factors which, in principle, can determine the scaling function. In Fig. 4.5, we compare the scaling functions for films and pores. From Fig. 4.5 we can find that, near T_λ, the scaling function for films and pores are different although their shapes are similar. Compared with the scaling function for films, the scaling function for pores shifts to the left, further away from the bulk behavior. This is expected, since in comparison with the film geometry, the pore geometry restricts the dimensionality of the system more, thereby further limiting critical fluctuations. As a consequence, the thermal resistivity for the pore geometry is higher at T_λ and decreases to 0 at lower temperature.

Chapter 5

Conclusions

We have calculated the thermal resistivity $R(\epsilon, H)$ of the XY model in a film geometry (on a $L \times L \times H$ lattice), which belongs to the same universality class as liquid ^{4}He. We applied periodic boundary conditions along the L directions and open boundary conditions in the H direction. We obtained the thermal resistivity scaling function $g(x)$ using known values for the critical exponents. We find good agreement for scaling functions between the results of the simulation and experiment for $x > -0.4 \times 10^{-5}$ using the temperature scale and the thermal resistivity scale as free parameters if we use $\chi = 0.4397$ determined by experiments[51]. If we use $\chi = \nu/2$, determined by dynamic scaling theory[50], agreement between simulation and experiment is good only for $x < -0.4 \times 10^{-5}$.

We also compared our calculated scaling function for a film geometry with that for a pore geometry and found a systematic shift.

In our simulation, we use open boundaries along the confining dimension (the H dimension). It has been demonstrated[23] that the boundary conditions play a significant role in defining the universal function. We believe that if we use more realistic boundary conditions, such as Dirichlet boundary conditions along the confining direction, we can reduce the number of fitting parameters to only one.

Part II

Bose Einstein condensation in a box trap: a Monte Carlo study

ABSTRACT

Recently Bose-Einstein condensates in a quasi-1d optical box trap has been produced in experiments, and the ground state of quasi-1d Bose gases in a hard-wall trap has been analytically studied. We have investigated the same system, Bose-Einstein condensates in a quasi-1d trap, using the path-integral Monte Carlo method. We used Gaussian wall or hard-wall trapping potential along the boundary of the box in order to mimic such a trap. The two-body interaction was described by a hard-sphere potential whose radius equals the s-wave scattering length. We have calculated the density profiles of the systems as a function of the temperature, the strength of the two-body interaction and the number of the atoms. At last, we compared the simulation results with the experimental and analytical results.

Chapter 6

Introduction

6.1 Bose-Einstein Condensation(BEC)

As described in Chapter 1, Bose - Einstein Condensation(BEC) was predicted in 1925 by Albert Einstein[1], who speculated that cooling bosonic atoms to a very low temperature would cause them to fall (or "condense") into the lowest accessible quantum state, resulting in a new form of matter. And the first "true" Bose Einstein condensates were created by Eric Cornell, Carl Wieman[2] and Wolfgang Ketterle[3] in 1995.

Since BEC was predicted, particularly since the achievement of experimental observation of BEC in magnetically trapped atomic vapors, this phenomenon has attracted considerable interest from experimental and theoretical researchers. In dilute or weakly interacting gases, $na^3 \ll 1$, where $n = N/V$ is the number density and a is the hard core diameter of the bosons, the Gross-Pitaevskii (GP) theory[53, 54], a mean field theory for the condensate wave function, has successfully described the extraordinary properties of the condensate. Dalfovo et al.[55] gave a good review of numerous successful applications of mean field theories in BEC in atomic gases. Recently it has also become possible to study Bose systems with tunable interactions, $na^3 \approx 1$[56, 57, 58]. This makes the study of BEC and the role of interactions in trapped Bose gases over a wide range of densities of direct interest to experiment.

6.2 MC studies of BEC systems

Some of the earliest applications of Quantum Monte Carlo (QMC) to problems in condensed matter involved the simulation of liquid helium[59, 60, 61]. Ceperley [62] wrote a review

of applications of the powerful path integral Monte Carlo (PIMC) method to the study of superfluidity and BEC in bulk liquid helium. He generalized Monte Carlo simulation techniques commonly used for classical systems to simulate boson systems, and showed the excellent agreement between the simulation results and the experimental measurements on helium. We will briefly introduce the PIMC methods in the next chapter.

Recently, Giorini et al.[63] have evaluated the ground state energy E/N and the condensate fraction N_0/N (N is the total number of atoms, N_0 is number of atoms at the ground state) at $T = 0$K for a uniform Bose gas over a wide density range($10^{-6} \leq na^3 \leq 10^{-1}$) using diffusion Monte Carlo methods. They found that the mean field results of E/N agree well with the diffusion Monte Carlo results in the density range $10^{-6} \leq na^3 \leq 10^{-3}$. However there are clear differences at higher densities $na^3 \geq 10^{-3}$ (helium density is $na^3 \approx 0.21$). The results were relatively insensitive to reasonable variation of the inter-boson potential suggesting that a hard sphere interaction potential can be used for a wide range of systems.

Krauth[64] applied QMC to BEC in a trap. He investigated the dilute, trapped, hard sphere Bose gas at finite temperatures using PIMC. He found repulsive interactions between the atoms tend to spread them out in the trap resulting in a lower average density compared to the noninteracting case. He also found that the condensed atoms are highly concentrated at the cener of the trap while the uncondensed or thermal atoms are dilute, spread out over a wide range and are well approximated by a classical ideal gas.

6.3 Dimensionality in BEC

The study of the effects of reduced dimensionality has attracted considerable interest in condensed matter physics and statistical physics, for example, quantum films of superfluid ^{4}He on surfaces, superfluid ^{4}He clusters, and superfluid ^{4}He confined in restricted geometries. Recently, the experimental realization of low-dimensional BEC trapped in an optical lattice has stimulated the investigation in a low-dimensional system both theoretically[55, 65, 66]

and experimentally[67, 68, 69, 70]. Dimensionally reduced systems have very different properties from their three-dimensional (3D) counterparts due to the enhanced importance of phase fluctuations[8, 9]. Nho et al.[71] investigated dilute Bose gases in a quasi-2D geometry in a harmonic trap. Their results show that the superfluid fraction for quasi-2D Bose gas decreases faster than that for a quasi-1D system and true 3D system with increasing temperature, and show a stronger dependence on the interaction strength.

Lower dimensional trapped Bose gases are usually realized with strong quantum confinement in one or more directions (i) by gradually reducing atoms from a highly anisotropic trap to decrease the interaction energy[67]; (ii) by gradually increasing the trap anisotropy while keeping the number of atoms fixed[68, 69]; (iii) by using the periodic potential of optical lattices[70].

6.4 BEC in a quasi-1D box boundary trap

Usually the external trap potential used in experiments and simulations are non-uniform, such as an harmonic trapping potential. In the trapped gas systems, the presence of an inhomogeneous external trapping potential means that the BEC has spatially dependent characteristics. As mentioned above[64], the condensed atoms are highly concentrated at the center of the trap. Recently T. P. Meyrath, et al. developed a new experimental approach[68] which has an optical box boundary trap. Two dimensions of the trap are strongly confined, while the other dimension is much larger than the confined dimensions. Thus the quasi-1d trap has relatively uniform distribution along the long dimension.

On the other hand, the ground-state properties of a trapped Bose gas in one dimension have been analytically studied recently by Y. Hao, et al.[72]. They calculated the density profiles of the gound state by solving Bethe ansatz equations numerically, and showed the effect of interactions between particles.

To compare with the experimental and analytical results, we use a finite-temperature path-integral Monte Carlo (PIMC) method to investigate a quasi-1D Bose-Einstein conden-

sate system in a box boundary trap, where the interparticle interaction is a purely repulsive hard-sphere potential of radius a_s, the s-wave scattering length. We will compare our accurate PIMC results with the simulation results for harmonic trap potential, the experimental results and the analytical results.

Chapter 7

Model and simulation method

In this chapter, we will give a review of the PIMC technique[62] and discuss all the necessary components required to build PIMC simulations. Starting from the thermal density, the path integral formalism will be introduced, and the role of permuting paths will be explained.

7.1 model

The system under investigation consists of N particles in a quasi-1d box, $x \times y \times z$, where $z \gg x, y$, in order to mimic the experiment. The model Hamiltonian reads,

$$\mathcal{H} = -\frac{\hbar}{2m} \sum_{i=1}^{N} \nabla_i^2 + \sum_{i=1}^{N} v_T(r_i) + \sum_{i<j}^{N} v_H(r_{ij}) \tag{7.1}$$

This Hamiltonian contains three terms. The first term is the kinetic energy. The second term is the trapping potential. We use hard-wall potentials or Gaussian wall potentials along the boundary of the box according to the invetigated systems. The Gaussian boundary trap potential has form

$$v_T(x, y, z) = ce^{-[(|x|-d_x)^2+(|y|-d_y)^2+(|z|-d_z)^2]/\sigma^2} \tag{7.2}$$

where c is some constant, (x, y, z) is the position of atoms, d_x, d_y and d_z are the dimension of the box range, $z >> x, y$, σ isthe variance of the Gaussian function. The hardwall boundary trap potential has form,

$$v_T(x, y, z) = c\delta(|x| = d_x \quad \text{or} \quad |y| = d_y \quad \text{or} \quad |z| = d_z) \tag{7.3}$$

The notation is the same as in Eq. 7.2. The third term is a two-body, symmetric hard-sphere potential defined by

$$v(r) = \begin{cases} \infty & (r < a_s) \\ 0 & (r > a_s) \end{cases}$$

where a_s is the s-wave scattering length. At ultralow temperatures, only the $l = 0$ partical wave scattering has contribution to the interatomic potential between two atoms. This spherically symmetric s-wave scattering governs the collisional properties of the system. Therefore we use s-wave scattering length, which describes the effective length scale of the scattering process, to model the interatomic potential.

7.2 Thermal density matrix

A quantum mechanical system in a pure state can be described by single wave function $|\Psi\rangle$, which can be expressed in terms of eigenvalues E_i and eigenfunctions $|\Psi_i\rangle$ of the Hamiltonian H. The corresponding density matrix operator is given by,

$$\rho = |\Psi\rangle\langle\Psi|. \tag{7.4}$$

The density matrix provides a convenient way to extend the study to finite temperature. Following the principles of statistical mechanics, if one assigns a classical probability p_i to the quantum mechanical state $|\Psi_i\rangle$, the thermal density matrix is,

$$\rho = \sum_i p_i |\Psi_i\rangle\langle\Psi_i|. \tag{7.5}$$

In thermal equilibrium at temperature T, the probability of a given state i being occupied is $e^{-\beta T}$, where $\beta = 1/k_B T$. The thermal density matrix now reads,

$$\rho = \sum_i e^{-\beta E_i} |\Psi_i\rangle\langle\Psi_i| = e^{-\beta \mathcal{H}}, \tag{7.6}$$

where $\mathcal{H}$ is the Hamiltonian operator.

The equilibrium value of an operator O is,

$$\langle O\rangle = \frac{\mathrm{tr}(O\rho)}{\mathrm{tr}(\rho)} = \frac{\mathrm{tr}(Oe^{-\beta E_i})}{\mathrm{tr}(e^{-\beta E_i})} = Z^{-1}\sum_i \langle\Psi_i|O|\Psi_i\rangle e^{-\beta E_i}. \tag{7.7}$$

where the partition function is,

$$Z = \mathrm{tr}(\rho) = \mathrm{tr}(e^{-\beta E_i}) = \sum_i e^{-\beta E_i}. \tag{7.8}$$

For the sake of numerical simulations, it is convenient to use the position-space density matrix, which is,

$$\rho(R, R^{'}; \beta) = \langle R|e^{-\beta\mathcal{H}}|R^{'}\rangle = \sum_i \Psi_i^*(R)\Psi_i(R^{'})e^{-\beta E_i}, \tag{7.9}$$

where $R = \mathbf{r}_1, ..., \mathbf{r}_N$ and $\mathbf{r}_i$ is the position of the ith particle.

The expectation value of operator O in the position-space representation becomes,

$$\langle O\rangle = Z^{-1}\int dRdR^{'}\rho(R, R^{'}; \beta)\langle R|O|R^{'}\rangle, \tag{7.10}$$

and the partition function is given by

$$Z = \int dR\rho(R, R; \beta). \tag{7.11}$$

7.3 Discrete path integrals

The underlying principle for the introduction of path integrals is the product property of the density matrix stating that the low temperature density matrix can be expressed as the product of high temperature matrices. In operators,

$$e^{-\beta H} = (e^{-\tau H})^M. \tag{7.12}$$

where $\tau = \beta/M$. In position space, Eq. 7.12 becomes,

$$\rho(R_0, R_M; \beta) = \int ... \int dR_1 dR_2 ... dR_{M-1}\rho(R_0, R_1; \tau)\rho(R_1, R_2; \tau)...\rho(R_{M-1}, R_M; \tau). \tag{7.13}$$

This expression is exact for any $M \geq 1$.

The reason for using the path integral is that the primitive approximation can be applied in the limit of high temperature. Thus, we shall be able to write down an explicit form for the low-temperature density matrix which, however, involves many additional integrals. Suppose the Hamiltonian can be split in two parts, $\mathcal{H} = \mathcal{H}_1 + \mathcal{H}_2$, the density matrix can be expressed using the following operator identity,

$$e^{-\tau(\mathcal{H}_1+\mathcal{H}_2)} = e^{-\tau\mathcal{H}_1}e^{-\tau\mathcal{H}_2}e^{-O(\tau^2)}. \tag{7.14}$$

As $\tau \to 0$, the terms with higher order of τ become smaller and thus can be neglected. This is known as the primitive approximation:

$$e^{-\tau(\mathcal{H}_1+\mathcal{H}_2)} \approx e^{-\tau\mathcal{H}_1}e^{-\tau\mathcal{H}_2}. \tag{7.15}$$

In position space, the primitive approximation is,

$$\rho(R_0, R_2; \tau) = \int dR_1 \langle R_0|e^{-\tau\mathcal{H}_1}|R_1\rangle\langle R_1|e^{-\tau\mathcal{H}_2}|R_2\rangle. \tag{7.16}$$

Hence we can approximate the exact density matrix by the product of the density matrices for $\mathcal{H}_1$ and $\mathcal{H}_2$ alone. So if we know the density matrix for $\mathcal{H}_1$, for example, kinetic energy, and the density matrix for $\mathcal{H}_2$, for example, potential energy, we can obtain the density matrix for the whole $\mathcal{H}$ approximately.

The partition function has the form

$$\begin{aligned} Z &= \int dR_0 \rho(R_0, R_M = R_0; \beta) \\ &= \int ... \int dR_0 dR_1 ... dR_{M-1} \rho(R_0, R_1; \tau)\rho(R_1, R_2; \tau)...\rho(R_{M-1}, R_M = R_0; \tau). \end{aligned} \tag{7.17}$$

With the integral, each particle turns into a "polymer". $R_M = R_0$ means the polymers are closed, i.e. they are ring polymers. In other words, each particle is a ring polymer; an exact representation of a quantum wavepacket. The thermodynamic properties of Bose systems are exactly equivalent to those of a system with interacting classical "ring polymer"[73]. This gives us a simple classical picture for a quantum system. When the temperature is high, the size of the polymers is small. As the temperature decreases, the length of the polymers increases. (See Fig. 7.1, and compare it with Fig. 1.2)

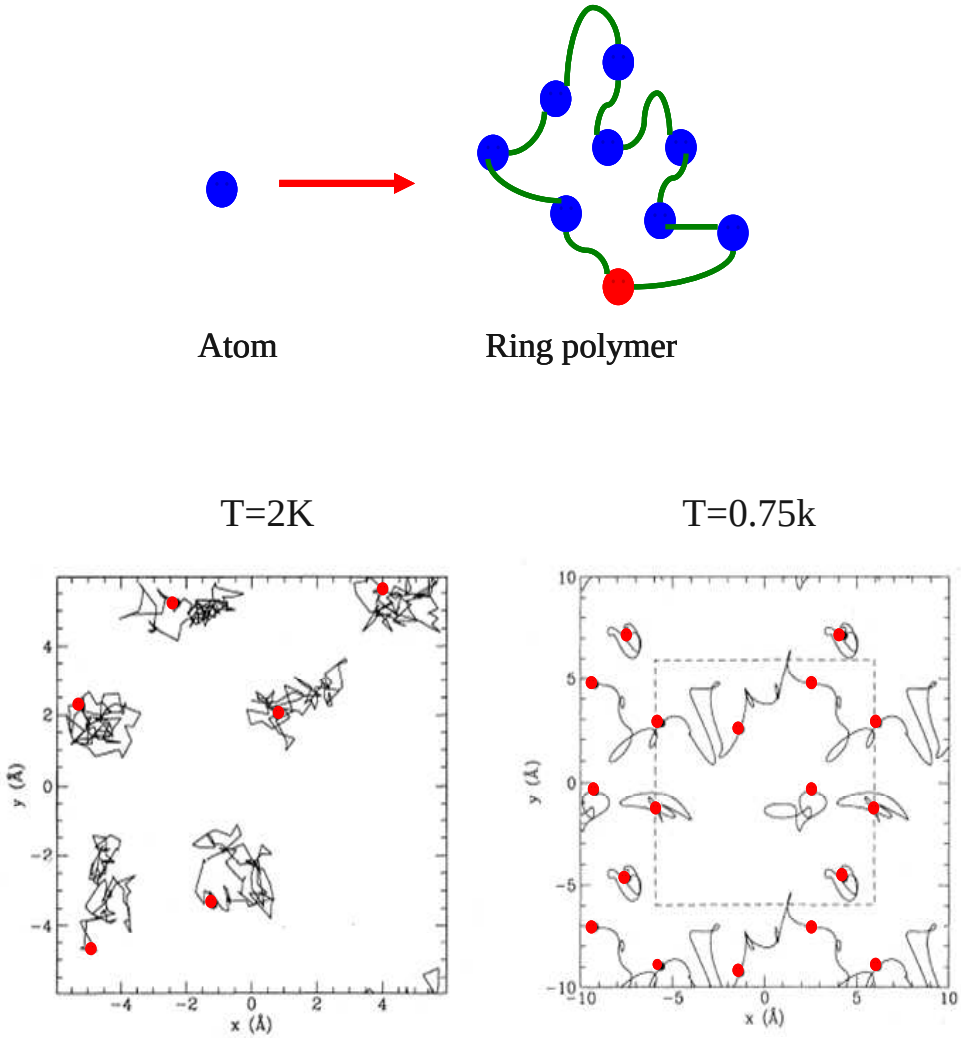

Figure 7.1: Each atom is a ring polymer. The red dots represent the "start" of the path. The lower the temperature is, the longer the polymers are. (From Dr. Ceperley's website)

7.4 Bose symmetry

The density matrices up to this point have been appropriate for distinguishable (Boltzmann) particle statistics, since the indistinguishability of particles was not taken into account. For a Bose system, only totally symmetric wave functions contribute to the density matrix. In other words, the wave functions must be symmetric under the exchange of two identical particles,

$$\Psi(R) = \Psi(PR) \tag{7.18}$$

where P stands for any of the $N!$ permutations of the particle labels, i.e. $PR = (\mathbf{r}_{P_1}, \mathbf{r}_{P_2}...\mathbf{r}_{P_N})$. This symmetry property can be realized by applying a symmetrization operator to wave functions for distinguishable particles,

$$P\Psi(R) = \frac{1}{N!}\sum_P \Psi(PR) \tag{7.19}$$

If we apply P to the density matrix, we will obtain the bosonic density matrix. Written in position space, this is

$$\rho_B(R_0, R_1; \beta) = \frac{1}{N!}\sum_P \rho(R_0, PR_1; \beta) \tag{7.20}$$

where ρ_B is the boson density matrix and ρ is the Boltzmann density matrix. One can apply the permutation to the first argument of ρ, or the last argument, or both. All three ways are equivalent and lead to the same results.

The symmetry enters into the path integral formulism as a sum over all $N!$ permutations. In addition to the integral over all configurations of paths, one has to sum over possible permutations of final set of coordinates R_M. Eq. 7.13 then reads,

$$\begin{aligned}\rho(R_0, R_M; \beta) &= \frac{1}{N!}\sum_P \int ... \int dR_1 dR_2 ... dR_{M-1} \\ &\quad \cdot\rho(R_0, R_1; \tau)\rho(R_1, R_2; \tau)...\rho(R_{M-1}, PR_M; \tau)\end{aligned} \tag{7.21}$$

The partition function for a Bose system then has the form

$$\begin{aligned}Z &= \textstyle\int dR_0(\text{right side of Eq.7.21}, PR_M = R_0) \\ &= \tfrac{1}{N!}\textstyle\sum_P \int ... \int dR_0 dR_1 ... dR_{M-1}\rho(R_0, R_1; \tau)\rho(R_1, R_2; \tau)...\rho(R_{M-1}, R_0; \tau)\end{aligned} \tag{7.22}$$

7.5 Density matrix for the investigated model

For the investigated system, we split the Hamiltonian into two parts, $\mathcal{H}_1$ includes kinetic energy and hard-sphere interaction, and $\mathcal{H}_2$ is the trapping potential energy.

$$\mathcal{H} = \mathcal{H}_1 + \mathcal{H}_2 = \{-\frac{\hbar}{2m}\sum_{i=1}^{N}\nabla_i^2 + + \sum_{i<j}^{N} v_H(r_i j)\} + \{\sum_{i=1}^{N} v_T(r_i)\} \tag{7.23}$$

Since the potential operator is diagonal in the position representation, its matrix elements are trivial:

$$\langle R_1|e^{-\tau\mathcal{H}_2}|R_2\rangle = e^{-\tau V_T(R_1)}\delta(R_2 - R_1). \tag{7.24}$$

For kinetic energy and the hard-sphere interaction, the density matrix is given in an analytical form[74]:

$$\langle R_0|e^{-\tau\mathcal{H}_1}|R_1\rangle = (\frac{m}{2\pi\hbar^2\tau})^{3/2}[e^{\frac{m(R_0-R-1)^2}{2\hbar^2\tau}} - \frac{a_s(\mu-a_s)}{R_0-R_1}e^{\frac{mD}{2\hbar^2\tau}}]. \tag{7.25}$$

where

$$\mu = (R_0 + R_1) \tag{7.26}$$

$$D = \mu^2 - 2a_s\mu + 2a_s^2 - 2a_s(\mu - a_s)\cos\chi \tag{7.27}$$

where χ is the angle between R_0 and R_1.

Using Eqs. 7.16, 7.21, 7.24,7.25 we arrive at the path integral expression for the density matrix of our investigated system in the primitive approximation:

$$\begin{aligned}\rho(R_0, R_M;\beta) &= \frac{1}{N!}\sum_P \int ... \int dR_1 dR_2 ... dR_{M-1}(\frac{m}{2\pi\hbar^2\tau})^{3/2} \\ &\times \prod_{m=1}^{M}[e^{\frac{m(R_0-R-1)^2}{2\hbar^2\tau}} - \frac{a_s(\mu-a_s)}{R_0R_1}e^{\frac{mD}{2\hbar^2\tau}}]e^{-\tau V_T(R_1)}.\end{aligned} \tag{7.28}$$

7.6 Multilevel metropolis method

It is easy to see that a staightforward evaluation of the density matrix Eq. 7.21 (or Eq. 7.28 for investigated system) is out of question, since there will be $N!$ permutations and $(M-1)$

order integrals. The way of dealing with this kind question is stochastically, as we mentioned in part I, using Monte Carlo methods to sample the integrand and permutations.

The total configuration space is made up of elements: $s = [P, R_1, ..., R_M]$ where $R_k = \mathbf{r}_{1k}, ..., \mathbf{r}_{Nk}$ are the path variables and P is the permutation that closes the path, $R_M + 1 \equiv PR_1$. According the partition function Eq. 7.22, we wish to sample these elements in the simulation from the probability distribution

$$\pi(s) = \frac{\exp(-\sum_{k=1}^{M} S^k)}{Z}, \tag{7.29}$$

where S^k is the action of the kth link defined as

$$S^k \equiv S(R_k - 1, R_k; \tau) \equiv -\ln[\rho(R_k - 1, R_k; \tau)]. \tag{7.30}$$

The partition function Z normalizes the function $\pi(s)$ in this space.

The straightforward idea is the Metropolis algorithm[38] with single slice move, i.e. a single atom at a single time slice is displaced. However, it is not efficient. The average displacement in a single slice move is of order $\sqrt{\tau}$, which means the diffusion through phase space goes to zero for small time steps. This is clearly an unwanted effect in particular because one would like to have an algorithm that is almost independent of the time step.

The efficiency of this method can be improved by a multilevel Metropolis method. Instead of moving at a single slice, one regrows a whole section of the path containing $2^k - 1$ slices. The number k is called the level of the move. The efficiency can be further improved by rejecting certain unlikely paths at an earlier level instead of waiting until the end and then using a single Metropolis step. The algorithm can be stated as follows:

1. One starts at the highest level k, samples the atoms according to T_k and accepts with probability

$$A(s_k \to s_k^{'}) = \min\{1, \frac{T_k(s_k^{'} \to s_k)\pi_k(s_k^{'})}{T_k(s_k \to s_k^{'})\pi_k(s_k)}. \tag{7.31}$$

   according to the detailed balance

$$A(s_k \to s_k^{'})T_k(s_k \to s_k^{'})\pi_k(s_k) = A(s_k^{'} \to s_k)T_k(s_k^{'} \to s_k)\pi_k(s_k^{'}) \tag{7.32}$$

where T is an "*a priori*" sampling distribution and A is an acceptance probability. The transition probability is $T \cdot A$.

2. If the move is rejected one starts again from the beginning.

3. Otherwise, one continues at the next level $k \to k-1$ and uses a modified acceptance probability,

$$A(s_k \to s_k^{'}) = \min\{1, \frac{T_k(s_k^{'} \to s_k)\pi_k(s_k^{'})\pi_{k+1}(s_k)}{T_k(s_k \to s_k^{'})\pi_k(s_k)\pi_{k+1}(s_k^{'})} \tag{7.33}$$

The algorithm as a whole satisfies detailed balance because it is fulfilled on each level. One advantage of this method is that unlikely moves are rejected early.

7.7 Bisection method

A good method to construct the path efficiently with the multilevel Metropolis method is the bisection method. Suppose a single-particle or many-particle path consisting of $m = 2^k - 1$ time slices is "clipped out" where k is the level. The fixed end points are R_i and R_{i+m}. The new points to be sampled will have the coordinates $R_i + 1, ..., R_{i+m-1}$. The places that pose the greatest difficulty for finding a new path are in the middle of the interval $R_{i+m/2}$, simply because the middle is the farthest from the end points, which are known to have acceptable potential energies. The coordinates are partitioned into levels.

The bisection algorithm is recursive. First the mid-point is sampled. Then the same algorithm is used to find the midpoints of two remaining intervals, etc. The coordinates to be moved are partitioned as

1. s_0 = atom positions outside of time slices in consideration and atoms not being moved.

2. s_1 = coordinates of atoms being moved at the middle time slice $i + m/2$.

3. s_2 = coordinates of atoms being moved at the middle time slice $i + m/4, i + 3m/4$.

4. repeat step(3) to the lowest level.

5. s_k = coordinates of atoms being moved at the middle time slice $i+1, i+3, i+m-1$.

7.8 Permutation sampling

Bose statistics requires to sum over all permutations in addition to integration in real space. It can be combined into one MC process that samples configurations in the space of coordinates and permutations. In this section, we describe how to pick the permutation.

As we discussed with regard to bisection, a set of $m-1$ time slices are selected for the path move with end points R_i and R_{i+m}, where $m = 2^k - 1$. A local permutation move consists of applying a cyclic exchange of N atoms to an existing path. Once the path is picked, the bisection algorithm is used to sample a path corresponding to that permutation exactly as before. We can regard the permutation change as the first level in the multilevel sampling method. The second level will be the midpoint of the interval, $R_{i+m/2}$, and so forth.

Since permutation space is discrete, we can directly use the optimal algorithm. For a permutational change, the heat-bath transition probability is

$$T(P) \propto \rho(R_i, PR_{m-1}; m\tau) \tag{7.34}$$

Terms involving the interaction potential and the trap potential do not change under particle interchange, therefore, they will drop out. In other words, $T(P)$ depends only on the free-particle kinetic action.

Since the normalization is known, one can use the heat bath transition rule, in which a permutation $P^{'}$ is sampled from the neighborhood $N(P)$ of the current permutation P using their equilibrium distribution,

$$T^{'}(P \rightarrow P^{'}) = \frac{T(P)}{C(P)}. \tag{7.35}$$

where the normalization is given by the sum over all neighboring states

$$C(P) = \sum_{P^{'} \in N(P)} T(P^{'}), \tag{7.36}$$

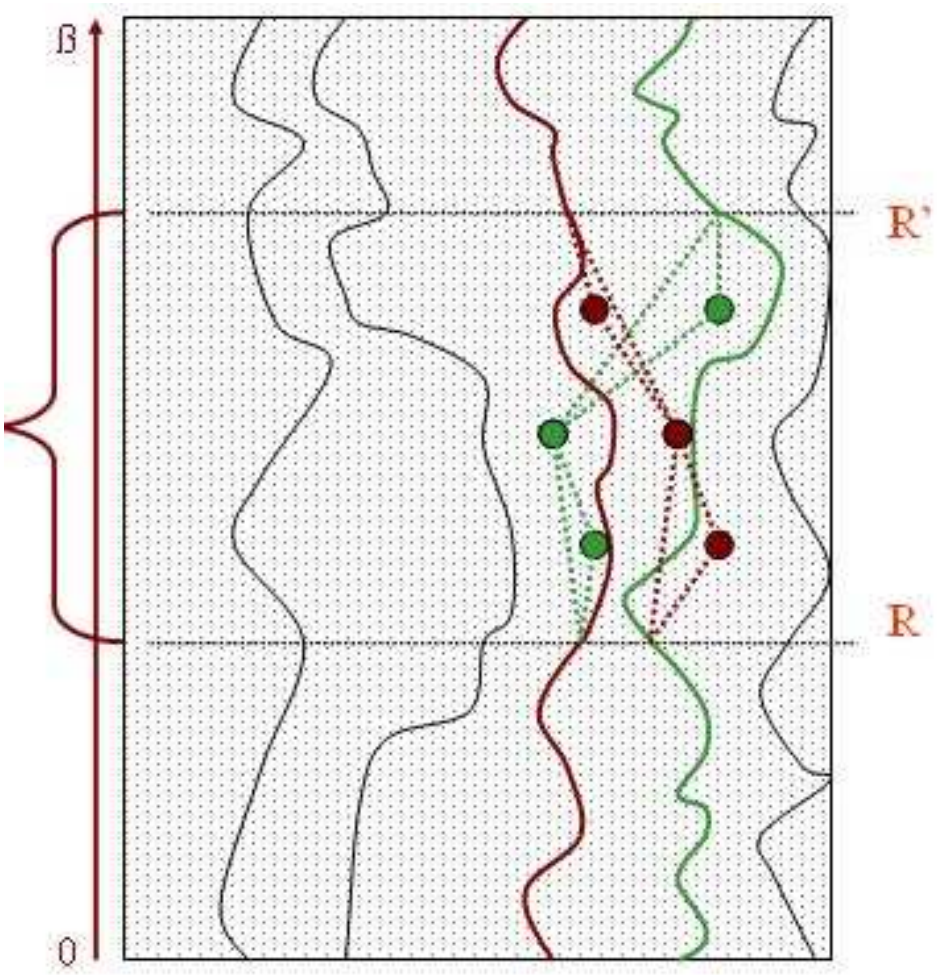

Figure 7.2: Bisection. Each curve represents a path of an atoms. (i) The two atoms permutate at slice R, (red and green). (ii) select another slice at $R^{'}$. Between R and $R^{'}$, there are $2^k - 1$ slices. Here $k = 2$. (iii) select midpoints at first level (the middle red and green dots). (iv) select midpoints at lowest levels (the top 2 and bottom 2 dots). (v) accept or reject the entire move. (From Dr. Ceperley's website)

The acceptance probability is

$$A(P \to P^{'}) = \min\{1, \frac{C(P)}{C(P^{'})}\}. \tag{7.37}$$

If the neighborhood of P and $P^{'}$ are equal, all moves will be accepted.

Since there are $N!$ permutations, it is advisable to put an upper limit on the step size in permutation space. Typically, one only considers changes in current permutations that involve the cyclic exchange of up to several particles. In our simulation, this limit is set to $N^{1/3}$.

7.9 Calculating properties

After the system reaches equilibrium with PIMC processes, we continue the Monte Carlo many steps, and record the positions of the particles at some processes for all slices. Now we are ready to calculate the properties of the system, such as the density profile and the energy of the system.

The density profile indicates the likelihood of finding particles at a distance r from a given origin. The density is simply the average over the paths. Since all time slices are equivalent, the average density is

$$\rho(r) = \frac{1}{M} \sum_{k=1}^{M} \sum_{i=1}^{N} \frac{\delta(r_{i,k} - r)}{r^2} \tag{7.38}$$

with

$$\int_0^\infty \rho(r) r^2 dr = 1 \tag{7.39}$$

where $r_{i,k}$ is the coordinate of particle i at slice k.

The other main property that one wants to get out of a simulation is internal energy.

The thermodynamic estimator of the energy is obtained by differentiating the partition function with respect to the inverse temperature,

$$E_T = -\frac{1}{Z} \frac{dZ}{d\beta}. \tag{7.40}$$

Interpreting the ratio as an average over imaginary-time paths, and applying the derivative to link i alone, we get

$$E_T = \frac{3N}{2\tau} - \frac{(R_i - R_{i-1})^2}{4\tau^2} + v_H + v_T. \tag{7.41}$$

The first two terms are the kinetic energy, the third term is the hard-sphere interaction potential, and the last term is the trapping potential.

The simulation has been performed on the IBM p655 high performance computer in the Research Computing Center at University of Georgia. The calculation runs on multiple processors with different random number simultaneously. To obtain the density profiles for system $N = 64$, $T = 0.4T_c$, the CPU time is about 5×10^6s. All error bars of the results correspond to one standard deviation.

Chapter 8

Results

In this chapter, we will show the results from the PIMC simulation for particles in a box trap potential, and compare the results to those using a harmonic trap potential, the experimental results and numerical analysis results.

8.1 Comparison of simulation results with boundary trap potential and harmonic trap potential

In this section, we will show the simulation results of the properties of BEC in a boundary trap, and compare them to those in a harmonic trap. We consider N hard-sphere bosons in a quasi-1d box trap, which has a Gaussian form along the boundary of the box. Our goal is to study the effects of interactions between particles and the temperature, and check the properties of the system.

In this study, we typically use N=8, 27 and 64 hard spheres because the permutation sampling in PIMC is efficient if $N = L^3$, where L is an integer number. We use different scattering lengths and a wide temperature range, i.e., $0.1 < T/T_c < 2.0$, where T_c is the transition temperature. The ratio of the long dimension to the short dimension of the box is 30.

We first discuss the density profiles at $T = 0.4T_c$ as a function of number of hard spheres and the s-wave scattering length. Fig. 8.1 shows the calculated density profiles $\rho(r)$ as a function of r for N=27 and 64 and $a_s = a_{Rb}, 10a_{Rb}$, where $\rho(r)$ is normalized such that $\int_0^\infty \rho(r) r dr = 1$ and $r = \sqrt{x^2 + y^2}$. From Fig. 8.1, we can find that the total density profile

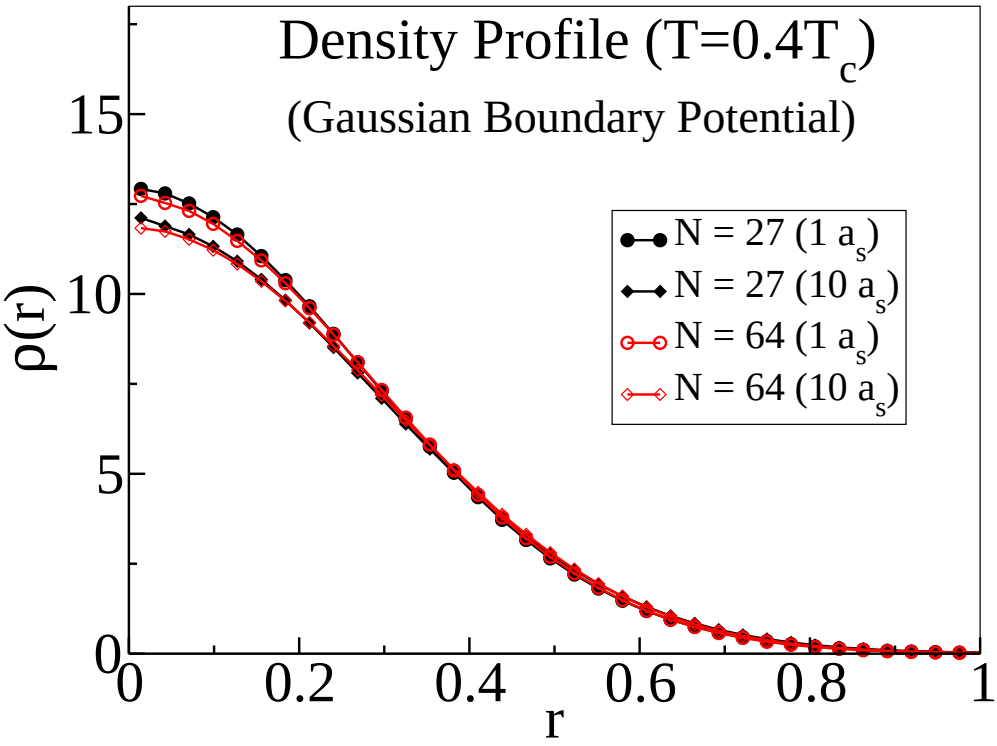

Figure 8.1: The calculated density profiles vs radial position r at $T = 0.4T_c$ as a function of number of hard spheres and the s-wave scattering length (in parentheses). The error bar is less than the size of the symbols.

along the r coordinate spreads out in the trap as both a_s and N increases, i.e. the density at the center of the trap decreases when increasing a_s and N.

Fig. 8.2 shows the calculated density profiles $\rho(r)$ as a function of r for a harmonic trap potential. We see that the effect of the number of hard spheres and the s-wave scattering length for Gaussian boundary potential and harmonic trap potential are qualitatively similar. However, the former is much weaker than the latter, because the particles for the Gaussian boundary potential are not as concentrated as that for harmonic trap potential.

To see the effect of the temperature T, we also calculated the density profiles $\rho(r)$ as a function of r for two different temperature $T/T_c = 0.4$ and $T/T_c = 1.5$ using two different

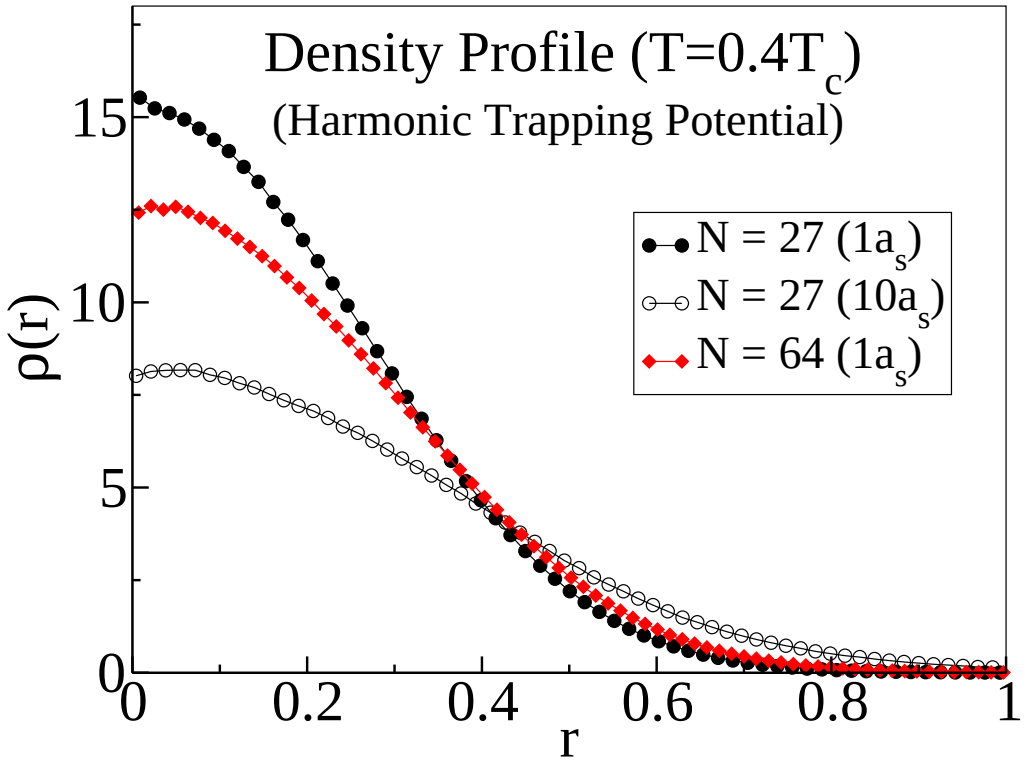

Figure 8.2: The calculated density profiles vs radial position r at $T = 0.4T_c$ as a function of number of hard spheres and the s-wave scattering length (in parentheses). The error bar is less than the size of the symbols.

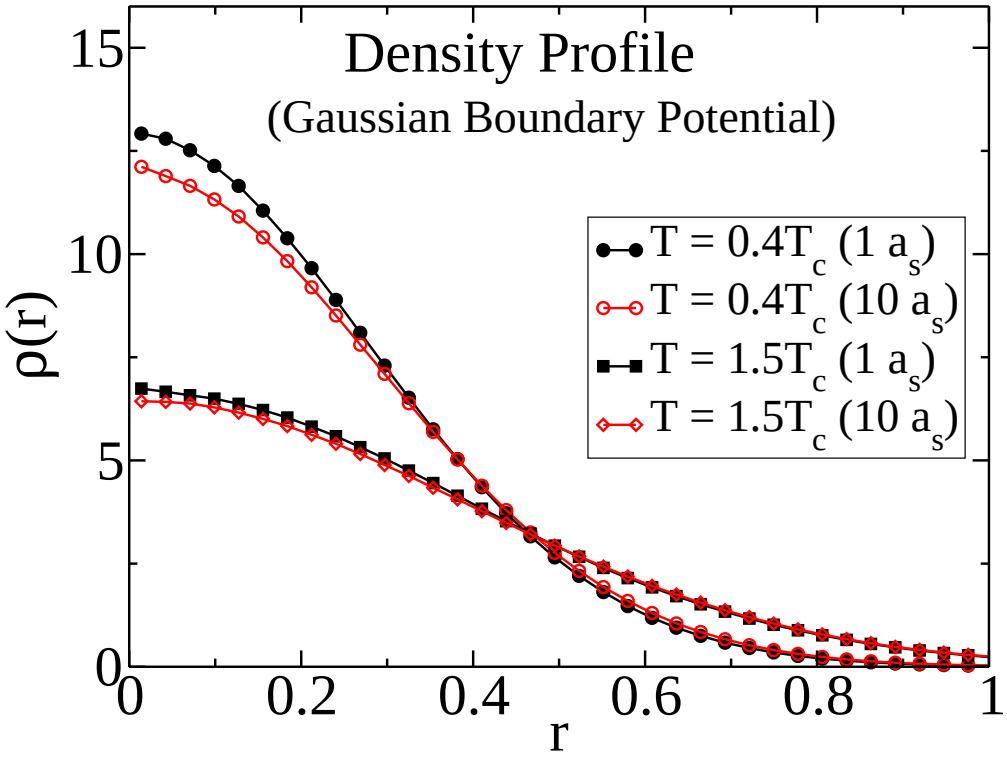

Figure 8.3: The calculated density profiles $\rho(r)$ for two different temperatures $T/T_c = 0.4$ and $T/T_c = 1.5$ using two different scattering lengths $a_s = a_{Rb}, 10a_{Rb}$.

scattering lengths $a_s = a_{Rb}, 10a_{Rb}$ (Fig. 8.3). As the temperature increases, the density profiles $\rho(r)$ expand along the r axis and the effect of the interaction decreases.

Fig. 8.4 shows the calculated density profiles $\rho(r)$ as a function of r for the harmonic trap potential. We see that the effect of the temperature and the s-wave scattering length for Gaussian boundary potential and harmonic trap potential are qualitatively similar. However, the former is much weaker than the latter, because the particles for Gaussian boundary potential are not as concentrated as that for the harmonic trap potential.

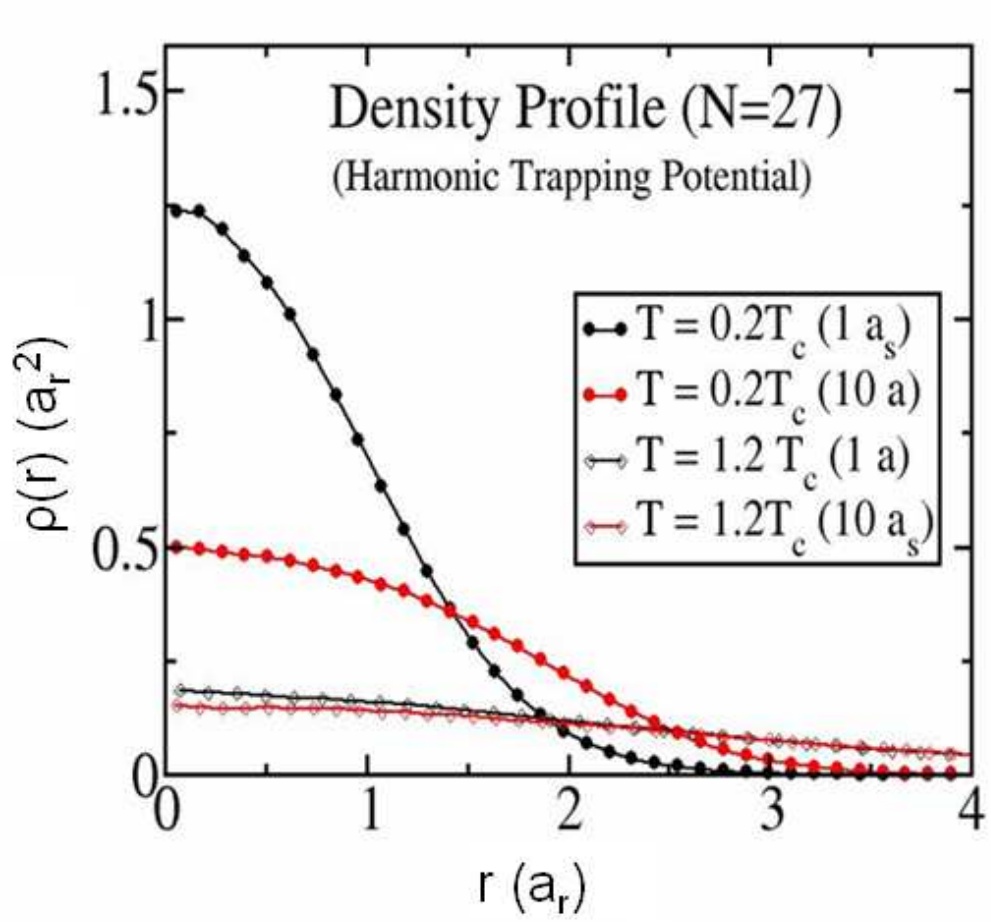

Figure 8.4: The calculated density profiles $\rho(r)$ for two different temperature $T/T_c = 0.4$ and $T/T_c = 1.5$ using two different scattering lengths $a_s = a_{Rb}, 10a_{Rb}$. (provided by K. Nho.)

8.2 Comparison of simulation results and experiment results

Mostly, the experiments for atom optics have relied on the use of optical lattices[75, 76, 77, 78]. Instead of a single lower dimensional condensate, many thousands are created in parallel.

Recently T. P. Meyrah et al.[68] developed a new experimental approach. The trap geometry is a quasi-1d box, the ratio of the longest and shortest dimensions is about 30. In the center range of the box, the potential is nearly 0. Near the boundary of the box is the Gaussian wall. With this kind of setup, along the two strong confined dimensions, it is samilar with those typically reported for optical lattices. However, along the long dimension, there is only a single condensate in 1d. Single atom detection with nearly unit quantum efficiency has been demonstrated, paving the way for direct measurements of quantum atom statistics.

Fig. 8.5 shows the experiment results with 3×10^3 atoms in the trap. Fig. 8.5 (a) is the absorption image of the BEC of 3×10^3 atoms in a box along the z axis. The absorption image is *in situ*, where the absorption beam is turned on. Resolution is limited by expansion during the 30μs exposure. Fig. 8.5 (b) is the profile of the BEC along the z axis.

In order to mimic the experiment, in the simulation, we use similar box geometry and trap potential. The number of atoms $N = 27$, which is enough for general qualitative comparison. The ratio of longest and shortest is $d_z/d_x = d_z/d_y = 30$, same with the experiment. The trap potential is Gaussian walls seperated by dimensions of the box (Eq. 7.2).

Fig. 8.6 shows the calculated density profiles $\rho(z)$ as a function of z for $N = 27$ and $a_s = a_{Rb}$. Near the boundary, the profiles decrease quickly because of the Gaussian boundary potential. However, in the large middle range, the density profiles are nearly uniform. Comparing to the experiment results, we find the results of simulation and experiment are qualitatively consistent.

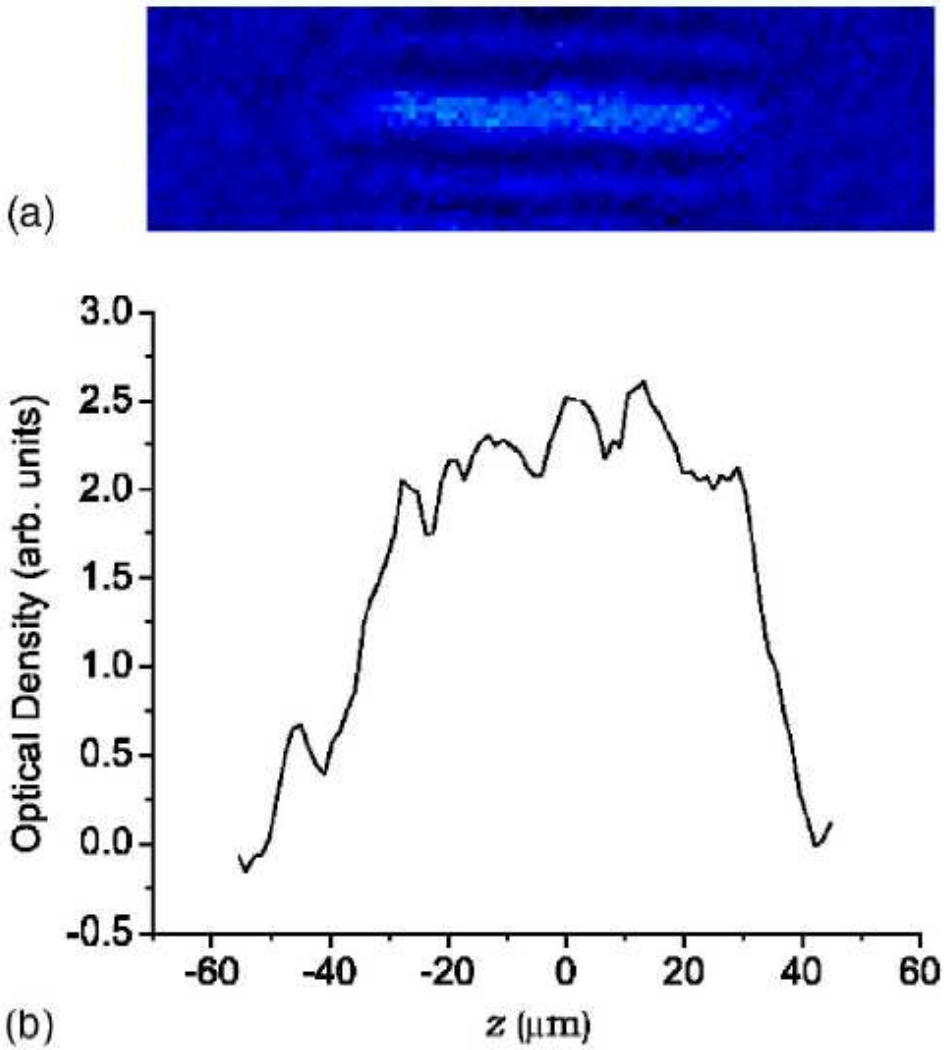

Figure 8.5: (a) The absorption image of the BEC of 3×10^3 atoms in a box along z axis. (b) The profile of the BEC along the z axis. The paper did not provide the error bar[68].

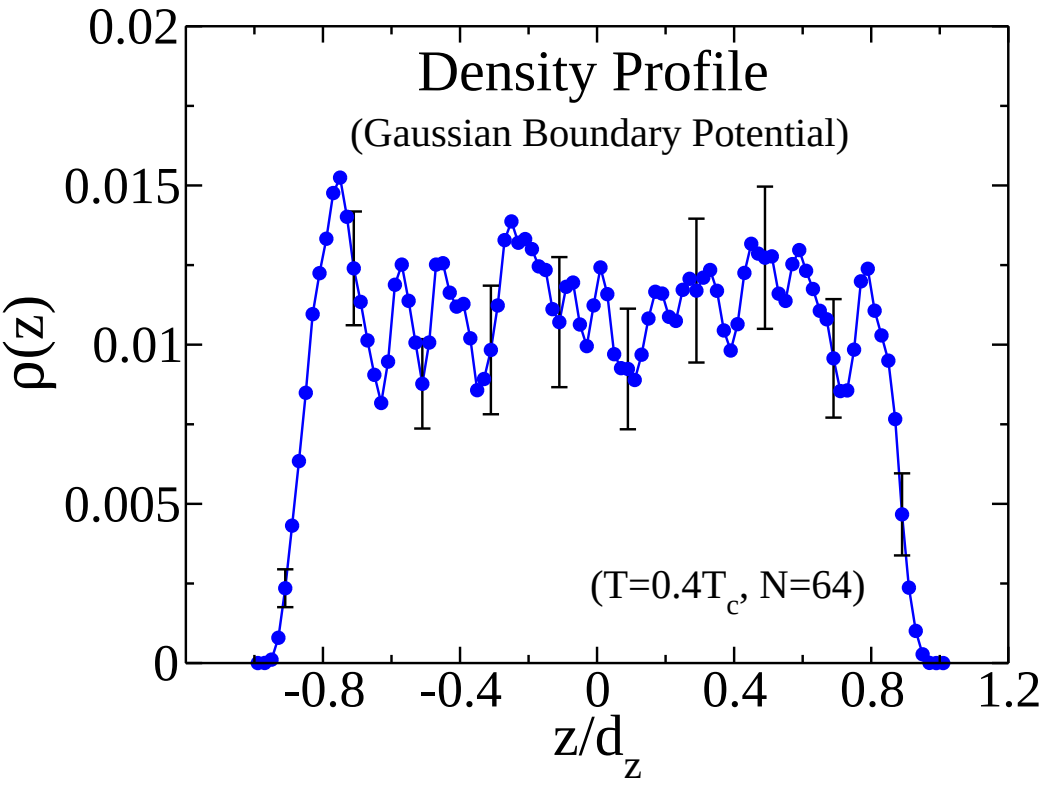

Figure 8.6: The calculated density profiles at $T/T_c = 0.4$ along z axis.

8.3 Comparison of simulation results and analytical results

As BEC in a quasi-1D box trap was generated in experiment, one may wish to know the theoretical solution. It is well known that there exist some exactly solved 1D interacting models[79, 80, 81] However, they are not directly applicable to the system trapped in an external harmonic potential. And the mean-field theory is only applicable in dealing with BEC system with very a weak interactions. Recently, Hao et al.[72] investigated the density distribution of the ground state of the 1D Bose gases in a hard-wall trap by numerically solving the set of Bethe ansatz equations. The hard-wall trap potential is give by

$$v_H = 2c\delta(x_i - x_j) \tag{8.1}$$

where $2c$ is the interaction strength between atoms. Fig. 8.7 shows the density profiles $\rho(z)$ of the ground state for different repulsive interaction constants and $N = 4$.

In the simulation, we let T be a very small value, 0.01K to approximate $T = 0$. The number of particles is 4, and the box geometry is the same as in the previous section. The hard-sphere interaction is applied. Although the relation between a_s and c is not known, we expect when $c = 0$, $a_s = 0$, and when $c \to \infty$, a_s approaches some constant. So to elucidate the effect of interactions, different scattering lengthes are used. Fig. 8.8 shows the simulated density profiles along the z axis. When there is no interaction between atoms ($a_s = 0$), the density profile is center-concentrated. As the interaction increases further, the half-width of the density of the system becomes larger and larger. When $a_s = 2$, the density distribution becomes oscillated because the interaction between atoms is strong such that the polymers of the atoms tend to be separated rather than overlaped.

To compare the analytical and simulated results directly, we put the analytical density profile for $c = 100$ and the simulated density profile for $a_s = 2$ on the same graph (Fig. 8.9). We see that their peaks and valleys correspond with each other and both of them show the effect of strong interaction obviously.

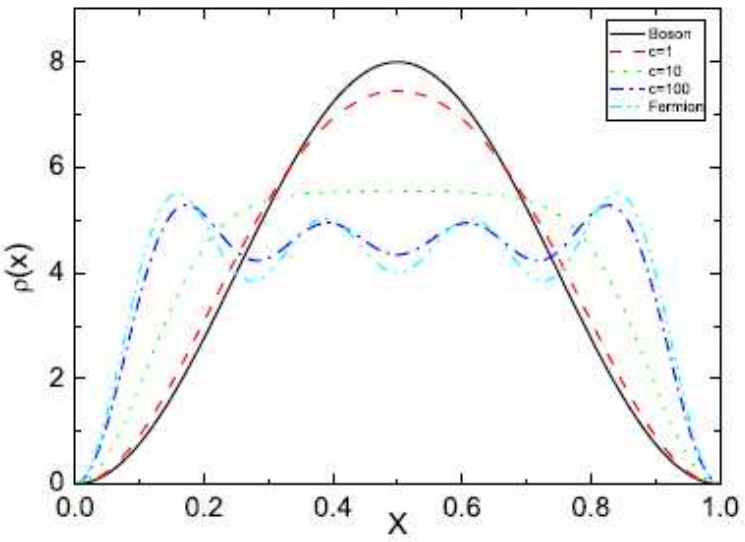

Figure 8.7: Numerical analyzed density profiles $\rho(x)$ of the ground state for different repulsive interaction constants, $N = 4$[72]. (The notation $\rho(x)$ is corresponding to our notation $\rho(z)$)

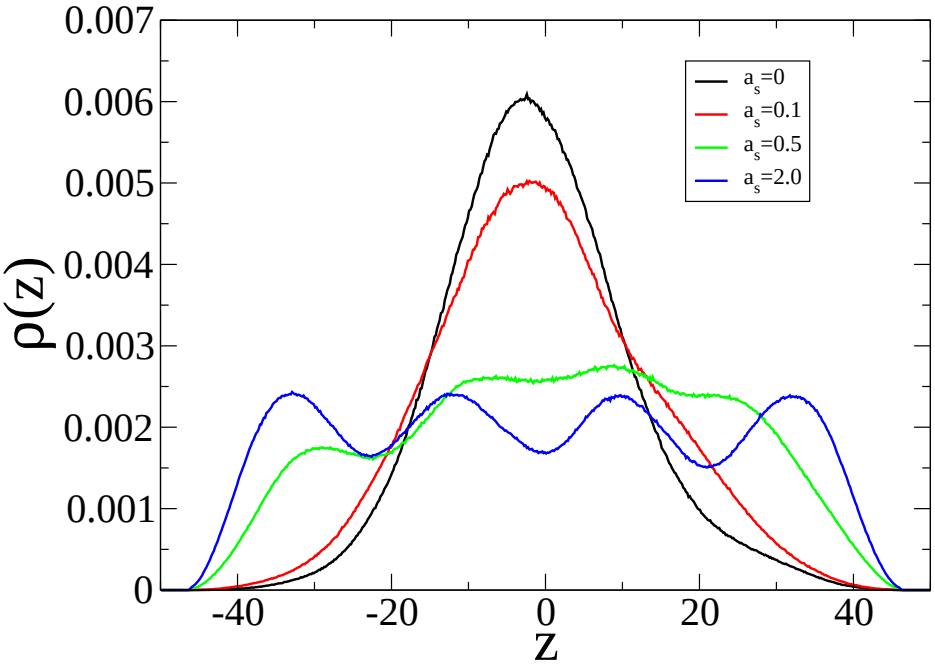

Figure 8.8: The simulated density profiles $\rho(z)$ for different interaction strength, $N = 4$.

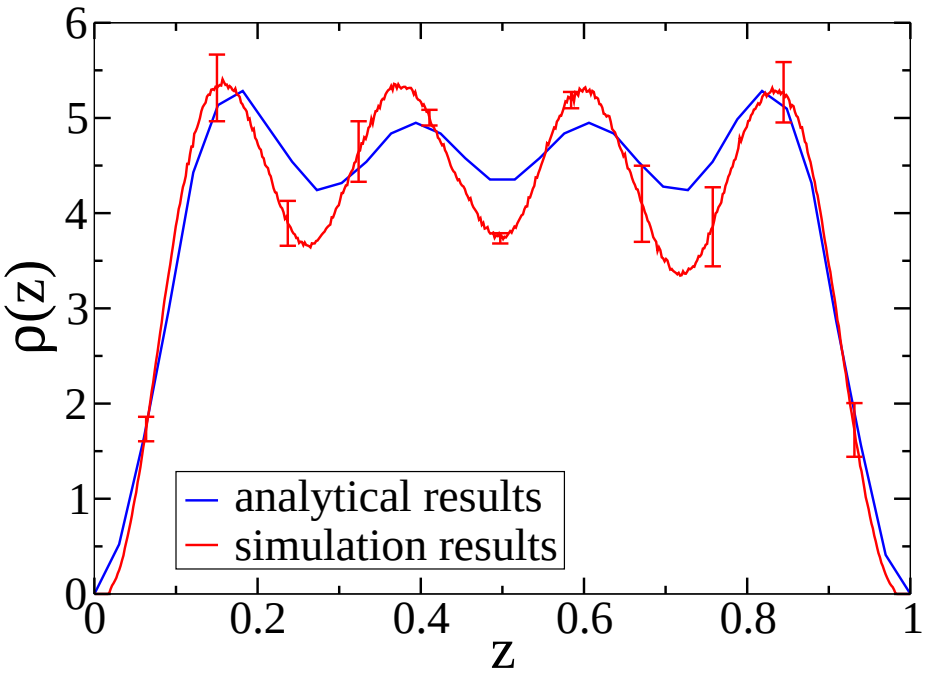

Figure 8.9: Comparison of the analyzed density profiles with $c = 100$ and the simulated density profiles with $a_s = 2.0$.

The amplitude of oscillations of the simulated density profile is larger than that of the analyzed density profile. The reason may be that the interaction for $a_s = 2$ in the simulation is stronger than that for $c = 100$ in the numerical method. If we let c become some bigger or a_s become some smaller, one can expect that both of them would be more consistent.

Chapter 9

Conclusions

In summary, using a finite-temperature path integral Monte Carlo technique (PIMC) we have investigated a Bose gas trapped by a Gaussian boundary potential or hardwall boundary potential in quasi-1D interacting via a hard sphere potential whose core radius equals its corresponding s-wave scattering length. We have presented and analyzed our PIMC results, such as the total energy and the density profile, as a function of temperature T/T_c at various values of the strength of the interaction and number of particles.

We have compared our simulation results to that with a harmonic trap potential. We find that for repulsive interactions, the density profile expands as the interaction strength increases. And the effect of interaction decreases when the temperature increases. These behaviors are the same as with the harmonic trap potential; however, the effect of repulsive interactions are much weaker than the case with the harmonic trap potential. This behavior is expected, because in a large range, the trap potential is 0 except near the boundary.

We also compare our simulation results with experimental results and numerical results. For this purpose, we try to make the systems as similar as possible. The results show good agreements between them qualitatively.

In the future, more works need to be done such that we can compare the results of simulation, experiment and numerical analysis more quantitatively and accurately. For example, what is the relation between a_s in the simulation and c in the numerical analysis, what is the effect of particle density, and so on. In addition, to investigated the effect of finite-size, we plan to calculated the properites of the systems for different sizes with same trap potentials and same particle density.

Bibliography

[1] A. Einstein. *Sitzungber. Preuss. Akad. Wiss.*, 23:3, January 1925.

[2] M. H. Anderson, J. R. Ensher, M. R. Matthews, C. E. Wieman, and E. A. Cornell. *Science*, 269:198, 1995.

[3] K. B. Davis, M. O. Mewes, and W. Ketterle. *Appl. Phys. B*, 60:155, 1995.

[4] P. Kapitza. *Nature (London)*, 141:74, 1938.

[5] J. F. Allen and A. D. Misener. *Nature (London)*, 141:75, 1938.

[6] F. London. *Phys. Rev.*, 54:947, 1938.

[7] F. London. *Nature*, 141:643, 1938.

[8] N. D. Mermin and H. Wagner. *Phys. Rev. Lett.*, 22:1133, 1966.

[9] P. C. Hohenberg. *Phys. Rev.*, 158:383, 1967.

[10] C. J. Pethick and H. Smith, *Bose-Einstein Condensation in Dilute Gases (CAMBRIDGE)*, 2002.

[11] M. E. Fisher and M. N. Barber, *Phys. Rev. Lett.* 28:1516, 1972; M. E. Fisher, *Rev. Mod. Phys.* 46:597,1974.

[12] E. Brezin. *J. Physique*, 43:15, 1982.

[13] S. Mehta and F. M. Gasparini. *Phys. Rev. Lett.*, 78:2596, 1997.

[14] S. Mehta, M. O. Kimball, and F. M. Gasparini. *J. Low Temp. Phys.*, 114:467, 1999.

[15] M. O. Kimball, S. Mehta, and F. M. Gasparini. *J. Low Temp. Phys.*, 121:29, 2000.

[16] J. A. Lipa, D.R. Swanson, J.A. Nissen, P.R.W.Z.K. Geng, D.A. Stricker, T.C.P Chui, U.E. Isrealsson, and M. Larson. *Phys. Rev. Lett.*, 84:4894, 2000.

[17] R. Schmolke, A. Wacker, V. Dohm, and D. Frank, *Physica B*, 165-166:575, 1990; V. Dohm, *Phys. Scr.*, T49:46, 1993.

[18] P. Sutter and V. Dohm, *Physica (Amsterdam)*, 194B-196B:613, 1994; W. Huhn and V. Dohm, *Phys. Rev. Lett.*, 61:1368, 1988.

[19] M. Krech and S. Dietrich, *Phys. Rev. A*, 46:1886, 1992; 46:1922, 1992.

[20] J. A. Nissen and T. C .P. Chui and J. A. Lipa, *J. Low Temp. Phys.*, 92:353, 1993.

[21] A. Wacher and V. Dohm. *Physica (Amsterdam)*, 194B-196B:611, 1994.

[22] N. Schultka and E. Manousakis. *Physica. B*, 194-196:537–538, 1994.

[23] N. Schultka and E. Manousakis. *Phys. Rev. Lett.*, 75:2710, 1995.

[24] N. Schultka and E. Manousakis. *Phys. Rev. B*, 52:7528, 1995.

[25] A. M. Kahn and G. Ahlers. *Phys. Rev. Lett.*, 74:944, 1995.

[26] K. Nho and E. Manousakis. *Phys. Rev. B*, 64:144513, 2001.

[27] J. A. Lipa, D. R. Swanson, J. A. Nissen, Z. K. Greg, P. R. Williamson, D. A. Stricker, T. C. P. Chui, U. E. Israelsson, and M. Larsen, *J. Low Temp. Phys.*, 113:849, 1998; Phys. Rev. Lett., 84:4894, 2000.

[28] W. Y. Tam and G. Ahlers. *Phys. Rev. B*, 32:5932, 1985.

[29] M. Dingus F. Zhong and H. Meyer. *J. Low Temp. Phys.*, 65:185, 1986.

[30] W. Y. Tam and G. Ahlers. *Phys. Rev. B*, 33:183, 1986.

[31] B. I. Hohenberg and E. D. Siggia, *Phys. Rev. Lett.*, 32:1289, 1974; *Phys. Rev. B*, 13:1299, 1976; E. D. Siggia, *Phys. Rev. B*, 13:3218, 1976; C. DeDominicis and L. Peliti, *Phys. Rev. Lett.*, 38:505, 1977; *Phys. Rev. B*, 18:353, 1978; R. A. Ferrell and J. K. Bhattacharjee, *Phys. Rev. Lett.*, 42:1638, 1979; *J. Low Temp. Phys.*, 36:165, 1979; P. C. Hohenberg, B. I. Halperin, and D. R. Nelson, *Phys. Rev. B*, 22:2373, 1980; V. Dohm and R. Folk, *Z. Phys. B: Condens. Matter*, 40:79, 1980; *Phys. Rev. Lett.*, 46:349, 1981; G. Ahlers, P. C. Hohenberg, and A. Kornblit, *Phys. Rev. Lett.*,46:493, 1981; *Phys. Rev. B*, 25:3136, 1982; V. Dohm and R. Folk, *Z. Phys. B: Condens. Matter*, 45:129, 1981; V. Dohm, *Phys. Rev. B*, 44:2697, 1991.

[32] D. Murphy, E. Genio, G. Ahlers, F. C. Liu, and Y. M. Liu. *Phys. Rev. Lett.*, 90:025301, 2003.

[33] E. Genio, D. Murphy, G. Ahlers, F. C. Liu, and Y. M. Liu. *Adv. Space Research*, 35:87, 2005.

[34] S. Jerebets, Y. M. Liu, F. C. Liu, and G. Ahlers. private communication.

[35] T. Matsubara and H. Matsuda, *Prog. Theor. Phys.*, 16:416, 1956; 16:569, 1956; 17:19, 1957.

[36] M. Krech and D. P. Landau. *Phys. Rev. B*, 60:3375, 1999.

[37] P. C. Hohenberg and B. I. Halperin. *Rev. Mod. Phys.*, 49:435, 1977.

[38] N. Metropolis, A. W. Rosenbluth, M. N. Rosenbluth, A. M. Teller, and E. Teller. *J. Chem Phys.*, 21:1087, 1953.

[39] U. Wolff. *Phys. Rev. Lett.*, 62:361, 1989.

[40] F. R. Brown and T. J. Woch. *Phys. Rev. Lett.*, 58:2394, 1987.

[41] A. M. Ferrenberg, D. P. Landau, and Y. J. Wong. *Phys. Rev. Lett.*, 69:3382, 1992.

[42] J. A. Plascak, A. M. Ferrenberg, and D. P. Landau. *Phys. Rev. E*, 65:066702, 2002.

[43] J. Frank, W. Huang, and B. Leimkuhler. *J. Comput. Phys.*, 133:160, 1997.

[44] M. Krech, A. Bunker, and D. P. Landau. *Comu. Phys. Comm.*, 111:1, 1998.

[45] H. Yoshida. *Phys. Lett. A*, 150:262, 1990.

[46] N. A. Lurie, D. L. Huber, and M. Blume. *Phys. Rev. B*, 9:2171, 1974.

[47] K. Nho and E. Manousakis. *Phys. Rev. B*, 59:11575, 1999.

[48] H. E. Stanley, *An Introduction to Phase Transitions and Critical Phenomena (Oxford University Press)*, 1971; M. E. Fisher, *Rev. Mod. Phys.*, 46:597, 1974.

[49] L. S. Goldner and G. Ahlers. *Phys. Rev. B*, 45:13129, 1992.

[50] R. A. Ferrell, N. Menyhard, H. Schmidt, F. Schwabl, and P. Szepfalusy. *Phys. Rev. Lett.*, 18:891, 1967.

[51] G. Ahlers. *J. Low Temp. Phys.*, 115:143, 1999.

[52] M. Topler and V. Dohm. e-print cond-mat/0212277.

[53] E. P. Gross. *Nuovo Cimento*, 20:454, 1961.

[54] L. P. Pitaevskii. *Sov. Phys. JETP*, 35:282, 1959.

[55] F. Dalfovo, S. Giorgini, L. P. Pitaevskii, and S. Stringari. *Rev. Mod. Phys.*, 71:463, 1999.

[56] S. Inouye, M. R. Andrews, J. Stenger, H. J. Miesner, D. M. Stamper-Kurn, and W. Ketterle. *Nature*, 392:151, 1998.

[57] J. Stenger, S. Inouye, M. R. Andrews, H. J. Miesner, D. M. Stamper-Kurn, and W. Ketterle. *Phys. Rev. Lett.*, 82:2422, 1999.

[58] S. L. Cornish, N. R. Claussen, J. L. Roberts, E. A. Cornell, and C. E. Wiemann. *Phys. Rev. Lett.*, 85:1795, 2000.

[59] W. L. McMillan. *Phys. Rev.*, 138(2A):A422, 1965.

[60] K. S. Liu, Kalos M. H, and G. V. Chester. *Phys. Rev. A*, 10:303, 1974.

[61] P. A. Whitlock, D. M. Ceperley, G. V. Chester, and M. H. Kalos. *Phys. Rev. B*, 19:5598, 1979.

[62] D. M. Ceperley. *Rev. Mod. Phys.*, 67:279, 1995.

[63] S. Giorgini, J. Boronat, and J. Casulleras. *Phys. Rev. A*, 60:2319, 1999.

[64] W. Krauth. *Phys. Rev. Lett.*, 77:3695, 1996.

[65] G. E. Astrakharchik, D. Blume, S. Giorgini, and B. E. Granger. *Phys. Rev. Lett.*, 92:030402, 2004.

[66] P. Ohberg and L. Santos. *Phys. Rev. Lett.*, 89:240402, 2004.

[67] D. Rychtarik, B. Engeser, H. C. Nagerl, and R. Grimm. *Phys. Rev. Lett.*, 92:173003, 2004.

[68] T. P. Meyrath, F. Schreck, J. L. Hanssen, C. S. Chuu, and M. G. Raizen. *Phys. Rev. A*, 71:041604, 2005.

[69] N. L. Smith, W. H. Heathcote, G. Hechenblaikner, E. Nugent, and C. J. Foot. *J. Phys. B*, 38:223, 2005.

[70] Z. Hadzibabic, S. Stock, B. Battelier, V. Bretin, and J. Dalibard. *Phys. Rev. Lett.*, 93:180403, 2004.

[71] K. Nho and D. P. Landau. *Phys. Rev. a*, 73:033606, 2006.

[72] Y. Hao, Y. Zhang, J. Q. Liang, and S. Chen. e-print cond-mat/0602483.

[73] R. P.Feynmann. *Phys. Rev.*, 90:1116, 1953.

[74] J. Cao and B. J. Berne. *J. Chem. Phys.*, 97:2382, 1992.

[75] B. Paredes, A. Widera, V. Murg, O. Mandel, S. Flling, I. Cirac, G.V. Shlyapnikov, T.W. Hnsch, and I. Bloch. *Nature*, 429:277, 2004.

[76] M. Greiner, O. Mandel, T. Esslinger, T. W. Hnsch, and I. Bloch. *Nature*, 415:39, 2002.

[77] T. Kinoshita, T. Wenger, and D. S. Weiss. *Scince*, 305:1125, 2004.

[78] B. Laburthe Tolra, K. M. O'Hara, J. H. Huckans, W. D. Phillips, S. L. Rolston, and J. V. Porto. *Phys. Rev. Lett.*, 92:190401, 2004.

[79] E. H. Lieb and W. Liniger. *Phys. Rev.*, 130:1605, 1963.

[80] C. N. Yang and C. P. Yang. *J. Math. Phys.*, 10:1115, 1969.

[81] J. B. Mcguire. *J. Math. Phys.*, 5:622, 1964.